NUMERICAL MODELING OF CONCRETE-FILLED FIBER-REINFORCED POLYMER PILES

by

Mostafa Jafarian Abyaneh

Submitted in partial fulfilment of the requirements
for the degree of Master of Applied Science

at

Dalhousie University
Halifax, Nova Scotia
September 2019

DEDICATION PAGE

I would like to thank my parents, Mehdi and Nasrin, and my twin brother, Mojtaba, for their endless love, support, and encouragement throughout my studies.

TABLE OF CONTENTS

LIST OF TABLES

LIST OF FIGURES

ABSTRACT

Although many studies have been conducted on the structural behavior of concrete-filled fiber-reinforced polymer (FRP) tube (CFFT), the soil-structure interaction of CFFT piles was not previously considered. In this study, a numerical model is developed to study CFFT pile behavior and interactions with soil foundation under lateral loading. The model, based on nonlinear finite element analysis (NFEA) and the disturbed state concept (DSC), considers material and geometrical nonlinearities as well as the interface of soil with the CFFT pile. The finite element model was verified against a full-scale field test from the literature conducted during the construction of a highway bridge. Based on deflection along the length of the pile, the model results are in good agreement with the experimental data. To investigate the effects of various parameters on the behavior of CFFT piles and local buckling, a parametric study was also performed on different geometrical and material properties, including the pile diameter to length ratio, FRP tube thickness, concrete strength, and soil properties. It was found that the surrounding soil and length to diameter ratio exerted the most noticeable influence, followed by concrete strength while the FRP thickness had the least impact on the results.

LIST OF ABBREVIATIONS AND SYMBOLS USED

A	Element area
A^c	Fully adjusted (FA) element area
A^i	Relatively intact (RI) element area
B	Strain interpolation matrix
c	Cohesion coefficient
C^e	Elastic stiffness matrix
C^{ep}	Elastoplastic stiffness matrix
C^{ep}	Elastoplastic stiffness matrix
CFFT	Concrete-Filled FRP Tube
D	Disturbance parameter
D	Pile diameter
DSC	Disturbed State Concept
D_u	Ultimate disturbance parameter corresponding to the failure
E_c	Concrete modulus of elasticity
F	Failure criterion function
f'_c	Concrete compressive strength
f'_t	Concrete tensile strength
F^c	Fully adjusted (FA) force
F^{exp}	Experimental force
F^i	Relatively intact (RI) force
FRP	Fiber-Reinforced Plastics
H	Hardening modulus

J_1	First invariant of stress
J_2	Second invariant of stress
J_{2D}	Second invariant of deviatoric stress
J_3	Third invariant of stress
J_{3D}	Third invariant of deviatoric stress
L	Length
MC	Mohr-Coulomb
N	Applied load per unit length
n	Flow rule
NFEA	Nonlinear Finite Element Analysis
p	Lateral pressure
Q_0	Applied load
Q_S	Friction load
S_0	Settlement
t	Thickness
u	Nodal displacement
w	Displacement in the radial direction
z	Depth
Δu	The increment of nodal displacement
$\Delta \varepsilon$	Strain increment
$\Delta \sigma$	Stress increment
ε	Strain
ε^e	Elastic component of strain
ε^p	Plastic component of strain

θ	Lode angle for Mohr-Coulomb failure criterion
λ	Positive Scalar parameter for plastic strain
σ	Stress
σ_1	First principal stress
σ_2	Second principal stress
σ_3	Third principal stress
σ_a	Axial stress at failure
σ^c	Fully adjusted (FA) stress
σ^{exp}	Experimental stress
σ^i	Relatively intact (RI) stress
σ_l	Lateral stress at failure
φ	Internal frictional angle
ψ	Residual stress

ACKNOWLEDGEMENTS

I would like to thank my co-supervisors Dr. Hany El Naggar, and Dr. Pedram Sadeghian for their support in my master's program.

CHAPTER 1 INTRODUCTION

In many geotechnical applications, shallow and deep soil reinforcements and foundations such as piles are utilized to prevent excessive deformation and failure of structures. In this research, the axial and lateral behavior of deep foundations was studied with emphasis on the interface of pile and granular soil. During the pile installation, stresses and strains are generated in the surrounding soil by two main mechanisms: the soil displacement and lateral friction. The soil displacement due to pile driving results in residual stresses in the soil surrounding the pile particularly in the radial and longitudinal directions.

Two fundamental types of piles can be defined based on their structural behavior including end-bearing and friction piles. In the case of end-bearing piles, the bottom end of end-bearing piles rests on a rock or high-strength soil. As a result, the end of the pile transfers loads from the structure to the soil. For friction piles, however, loads are transferred from the structure to the soil by the interface between the pile and the soil. An important factor in the design of friction pile foundations is the soil-structure interface in different soil layers. Conventional materials to fabricate piles include concrete, steel, and wood. However, using these construction materials in harsh environment often results in deterioration and corrosion in the pile which increases the long-term maintenance costs (Iskander et al., 2002). Therefore, the pile core can be protected by fiber reinforced polymers (FRP). The main focus of this research is on precast concrete-filled FRP tube piles in which the FRP tube serves as permanent lightweight non-corrosive formwork and a reinforcement element for concrete.

The pile analysis fundamentally depends on empirical correlations based on experimental observations from laboratory and full scale in-situ testing. In either case, the investigations are often carried out using instrumented piles leading to a direct quantification of the shaft friction and base pressure. The proposed empirical correlations allow to approximately quantify the expected bearing capacities of piles embedded in different types of soils; however, they are not

able to provide an assessment of the associated deformation patterns of embedded pile as well as surrounding soil. Hence, numerical modeling based on finite element analysis (FEA) is often adopted to achieve a deeper understanding of pile behavior, soil movement and especially the mechanical behavior of the soil–pile system.

1.1 Research Scope

The numerical model was composed of four phases including:

- **Phase 1**: Background and theory of numerical modeling of FRP piles using nonlinear finite element analysis (NFEA) and disturbed state concept (DSC)
- **Phase 2:** Numerical modeling of FRP piles under lateral loading in the MATLAB software
- **Phase 3:** Verification of numerical results with the experimental data obtained from a previous case study conducted on the route-40 bridge in Virginia
- **Phase 4:** Verification of numerical results with the experimental data conducted on the route-40 bridge in Virginia

1.2 Research Objectives

The objectives of this research are:

- To develop a numerical model for CFFT pile by using disturbed state concept (DSC)
- To calibrate the interface parameters with the experimental results from an in-field case study
- To perform a parametric study with different geometrical and material parameters

1.3 THESIS LAYOUT

The thesis contains the following chapters:

- **Chapter 1 - Introduction:** introduced a background for the research.

- **Chapter 2 - Literature Review:** provides a literature review on the previous studies regarding different pile types, focusing on the structural performance of FRP piles along with the friction and bearing behavior of the soil-pile interface.

- **Chapter 3 - Nonlinear Finite Element Analysis:** presents the first phase of the research which focuses on background and theory of numerical modeling of FRP piles using nonlinear finite element analysis (NFEA) and disturbed state concept (DSC).

- **Chapter 4 - Calibration and Parametric Study:** presents the second phase of the research which deals with numerical modeling of FRP piles under lateral loading in the MATLAB software. The results were then verified and caliberated with the experimental data obtained from a previous case study conducted on the route-40 bridge in Virginia. Moreover, a parametric study was also conducted on the corresponding pile with different parameters.

- **Chapter 5 - Conclusions and Recommendations:** In this chapter, a summary of the numerical modeling has been provided along with conclusions based on the modeling results.

CHAPTER 2 LITERATURE REVIEW

The design lateral load typically controls the sizing of deep foundations in bridges and offshore structures. In addition, the effective stresses for driven piles at the interface of soil and pile will be lower than precast piles since large lateral movements of a pile during impact driving can cause yielding of the surrounding soil leading to reduction in pile shaft resistance (L. M. Zhang & Chu, 2012). Different methods have been proposed in the literature to predict the lateral capacity of single pile including: p–y curve method (Matlock, 1970; Reese et al., 1974), elastic solution (Poulos & Davis, 1980), strain wedge model (Ashour et al., 2004), and finite element (FE) method (Brown & Shie, 1990; Comodromos & Pitilakis, 2005; Isenhower et al., 2014; Muqtadir & Desai, 1986; Trochanis et al., 1991; Yang & Jeremić, 2002). In this chapter, a literature review has been presented regarding the experimental and numerical studies conducted on different types of piles.

2.1 STATIC LOADING

Abu-Farsakh et al. (2017) developed finite element (FE) model in Abaqus for three different pile group (PG) configurations: vertical, battered, and mixed. The tests were conducted under static lateral load test of M19 pier foundation applied incrementally up to 848 t (Abu-Farsakh et al., 2011; Souri et al., 2015) as shown in Figure 2.1. The foundation was composed of 0.9 m square prestressed concrete piles organized in 4 × 6 configuration, which were inclined at 1H:6V slope. Two separate meshes were developed for pile and soil by using the eight-node linear continuum brick elements. The number of elements was approximately 10,500 for the pile mesh and 72,000 for the soil mesh. The soil domain boundaries were far away from the piles to diminish their influence on the response. The battered piles showed the highest lateral stiffness followed by mixed and vertical piles. Furthermore, the soil resistance influence depth was shallower for battered piles as compared to vertical piles.

Suleiman et al. (2015) investigated soil–pile interaction behavior of a single laterally loaded pile using a fully instrumented test on a precast concrete pile with diameter and length of 102 mm and 1.42 m, respectively. The pile was installed in well-graded sand and equipped with displacement transducers, shape acceleration array, strain gauges and thin tactile pressure sheets. In the case of short, stiff laterally loaded piles installed in cohesionless soils, the measured normalized maximum soil–pile interaction pressures showed a good alignment with the normalized pressures provided in the literature (Prasad & Chari, 1999). The soil movement near the pile extended up to 6.3 pile diameters (6.3D) from the center of the pile. A maximum soil heave of 20 mm was also observed, with the heaved soil zone extending to 5.4D from the center of the pile.

The energy-based solutions for pile foundations under lateral load were reviewed by Han et al. (2017) using a semi-analytical approach. By using the principle of minimum total potential energy, a system of differential equations for the pile deflection and soil displacements was derived. Based on the principle of minimum total potential energy or the principle of virtual work, a system of differential equations for the pile deflection and soil displacements was derived. Each individual governing equation can be solved either analytically or numerically using the FEM or finite-difference method in addition to an iterative solution scheme. Profiles of pile deflection, shear force, bending moment and soil displacements throughout the domain were obtained from the results of the energy-based analyses. Moreover, a stiffer pile response was observed when pile head rotation constrained to be zero.

2.2 Cyclic Loading

Allotey and El Naggar (2008) and Heidari et al. (2014) proposed a numerical model to evaluate the effects of gapping and soil cave-in and recompression on the lateral cyclic behavior of pile embedded in soil along with case studies of reinforced concrete piles under cyclic lateral loading.

Base on the results, soil cave-in and recompression decrease pile maximum moment, move its point of occurrence closer to ground surface, and increase hysteretic energy dissipation. Furthermore, the formation of gapping in cohesive soil leads to higher lateral displacement of the pile head and maximum bending moment of the pile shaft.

Zhang and Chu (2012) conducted a lateral-loading test on four driven steel H-shape piles with lengths up to 164.5 m in a marble area located in Hong Kong to evaluate the effect of pile verticality on the pile capacity. Large lateral movements of a pile during impact driving can result in yielding of the surrounding soil leading to a noticeable decrease in effective stresses between the soil and the pile wall. The site layers were composed of highly variable rockhead contours and deep depressions filled with weak soil deposits. The maximum lateral pile movement during driving was up to 8.7 m at a depth of 100 m, and the maximum local pile inclination angle reached 0.139, which was measured with the depth intervals of 0.5 m by using an inclinometer casing. The lateral movements of the piles during driving well matched the rock-head inclination and soil conditions as one of the results is shown in Figure 2.2.

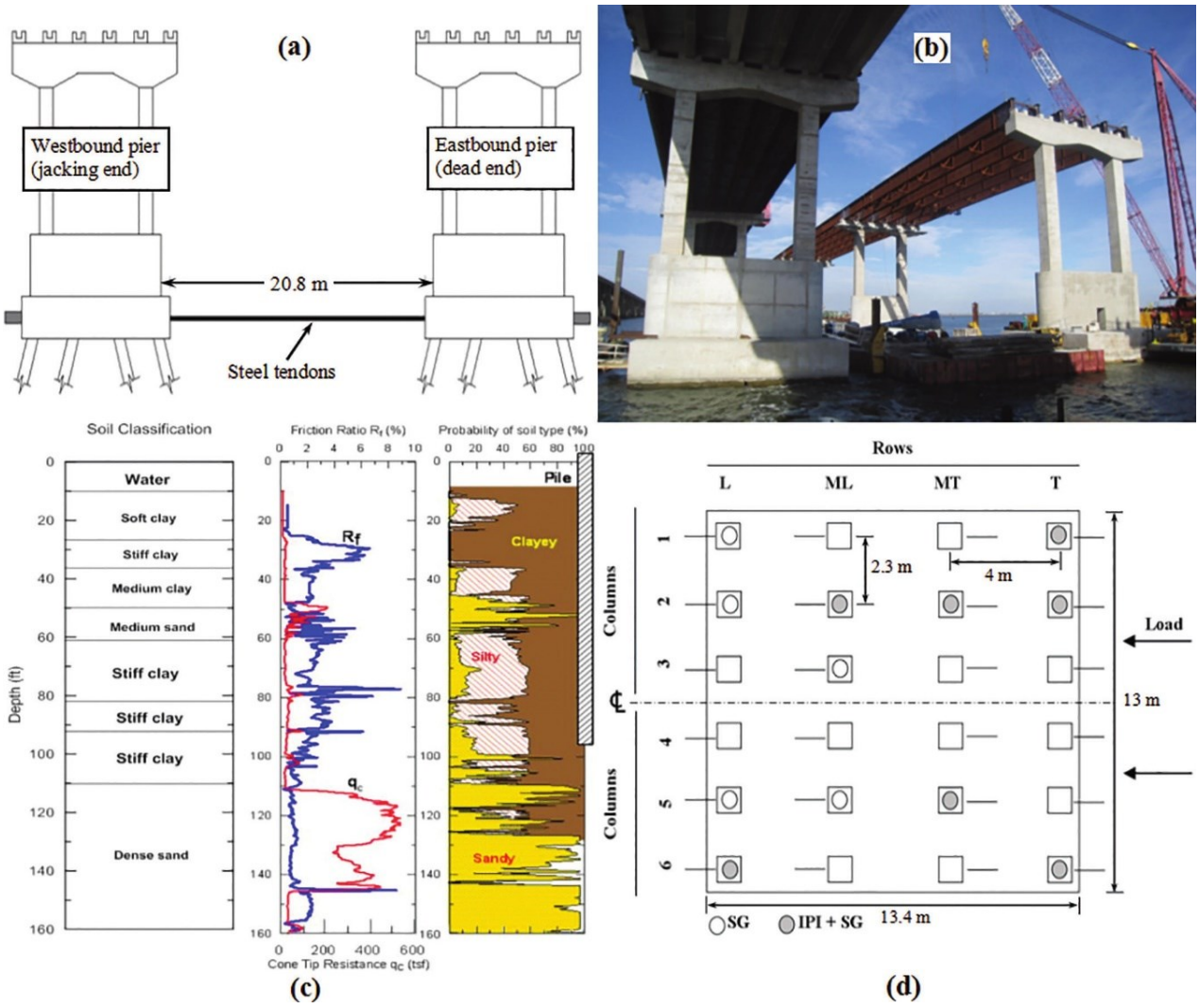

Figure 2.1 (a) Illustration for the lateral load test of M19 pier foundation, (b) test site, (c) soil layering and cone penetration test profiles, and (d) pile cap plan and pile labeling (Abu-Farsakh et al., 2017).

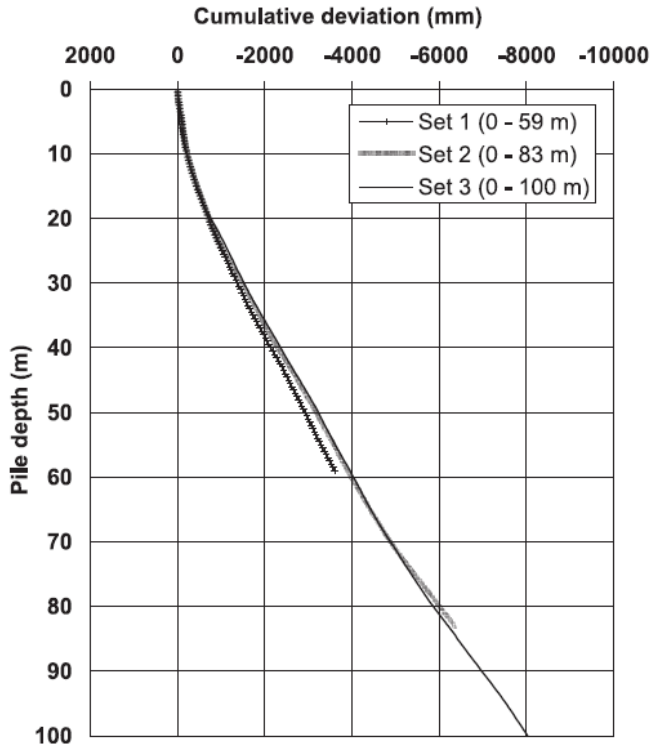

Figure 2.2 Horizontal displacement of a pile in the horizontal direction along the pile length (L. M. Zhang & Chu, 2012).

2.3 Optimum Pile Length

Leung et al. (2010) investigated the effect of pile length to optimize the overall foundation performance. The results of the research can be applied to piles with major frictional resistance to achieve economic and environmental savings. Consequently, an optimized pile length configuration can increase the overall stiffness of the foundation in addition to reduction in differential settlements that may cause distortion and cracking of the superstructure.

Chae et al. (2004) conducted experimental and numerical studies on a laterally loaded short pile and pier foundation located near slopes. The results of model tests of single piles and pile groups subjected to lateral loading in homogeneous sand with 30° slopes were modeled by the three-dimensional (3D) elastic–plastic finite-element method (FEM). Furthermore, different cases of

single short pile tests were carried out to study the effect of horizontal distance from the pile to the crest of the slope. In short pile groups, the focus was placed on the pile group efficiency and the behavior of each pile, considering the influences of the pile spacing and the pile cap. Based on the results, the lateral strength of the single short pile decreases, as its location is closer to the slope surface. In the case of short pile group near the crest of a slope, a noticeable reduction in the group efficiency was observed by the increase in the displacement.

2.4 Soil-Pile Interaction

Suleiman et al. (2014) investigated the interaction of well-graded sand and concrete pile subjected to lateral soil movement by using displacement and tilt gauges at the pile head and strain gauges, a flexible shape acceleration array, and thin tactile pressure sheets along the pile length (Figure 2.3). Diameter and length of the precast concrete pile were 102 mm and 1.58 m, respectively. The three-dimensional (3D) movements of the top level of the pile with respect to the soil surface were monitored using two stereo digital image correlation (DIC) systems. The soil-pile interaction was monitored by using the DIC instrument as the lateral displacement of the soil increases. Based on the results, a linearly increasing pressure is applied by the moving soil along the pile length above the sliding surface. The measured data was used to develop the soil-pile interaction force versus displacement (i.e., p-y curves) for the passive loading condition.

2.5 Loading Condition

Bohn et al. (Bohn et al., 2015) proposed new transfer curves based on a database of 50 instrumented pile load tests without the need for pressure-meter tests as opposed to the existing transfer curves. The existing curves were first compared to the measurements at the pile shaft and at the tip. Then the parameters of the most appropriate curve were calibrated to provide a single set of parameters applicable for most pile and ground types. The curves resulted from this method

were in good agreement with the overall load-settlement curve of 72 pile load tests. Figure 2.4 shows the curve at the tip and shaft of a pile from the mentioned pile load tests.

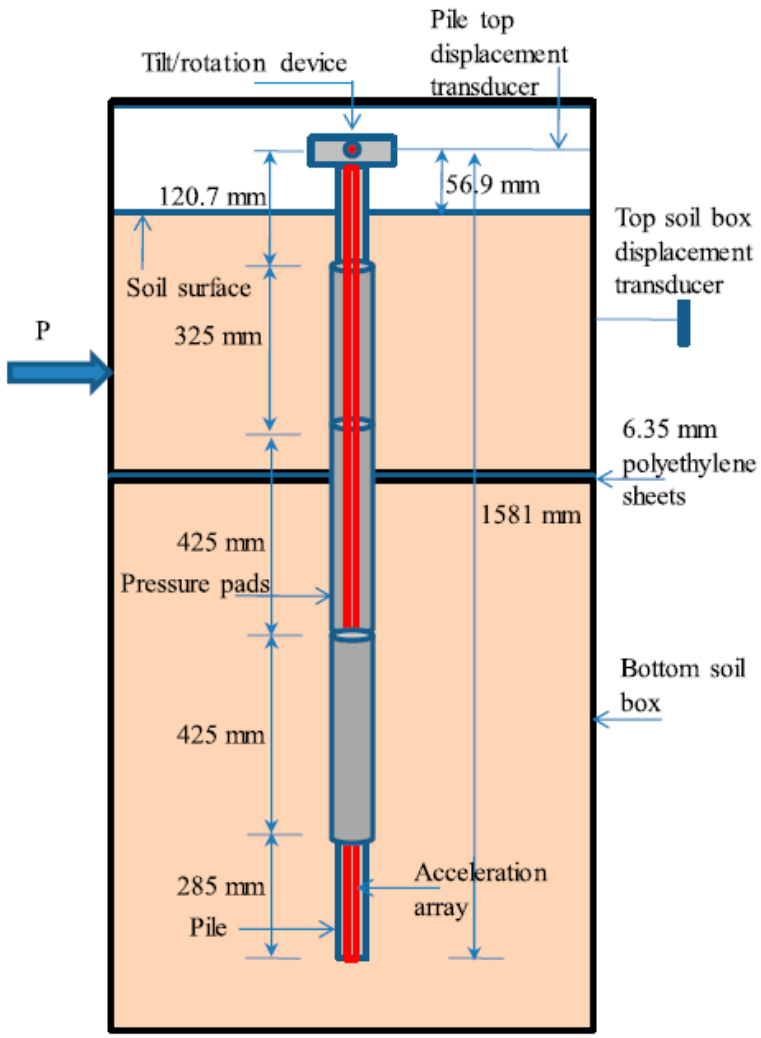

Figure 2.3 Instrumentations of the soil-pile system including the two soil boxes with the loading setup, displacement, rotation, pressure sheets, and acceleration array instrumentation (Suleiman et al., 2014).

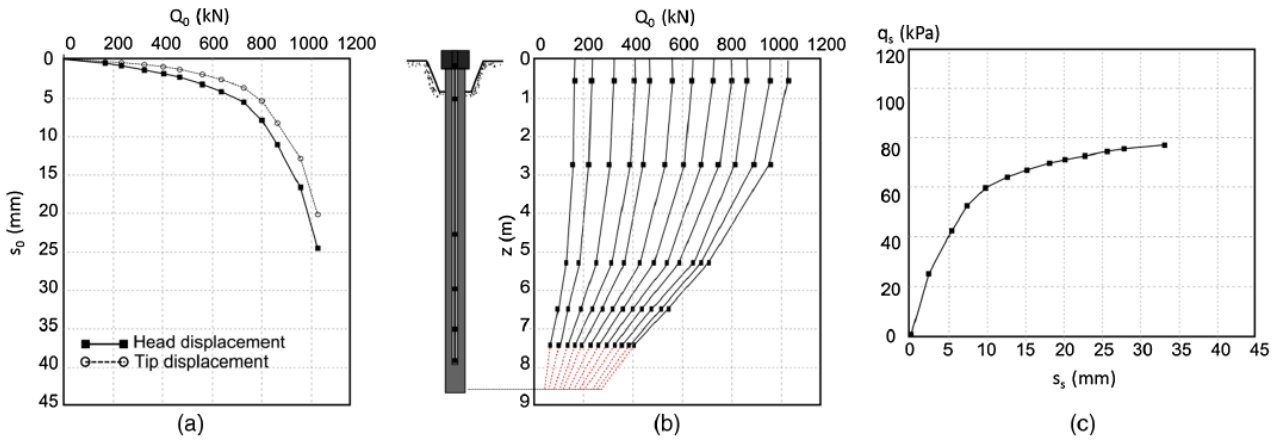

Figure 2.4 Main results of an instrumented load test with removable extensometer: (a) load-settlement curve for head and tip; (b) shaft load distribution between blockers and extrapolation for tip load; (c) skin friction load transfer curve (Bohn et al., 2015).

Dias and Bezuijen (2018) presented a framework for pile analysis leading to a discrete formulation applicable to different properties along the pile depth as well as any profile of soil settlements which is the case in deep excavations. For calibration of the model, a field load test was used to illustrate the benefits of including the unloading path and the relative settlement variable. The axial stress curve of the test versus the depth of pile has been depicted in the Figure 2.5, which shows a good agreement with the experiment.

Su and Zhou (2015) determined the effects of the loading direction on the behavior of laterally loaded pile groups by using a comprehensive experimental study. Pile groups with various configurations embedded in sand were subjected to lateral loads along different horizontal directions. The results show that the loading direction has a predominant effect on the evolution and eventual distribution of force among piles in the pile group, the bending responses along the piles, and the total lateral resistance of the pile group. The effect of the loading direction on the behavior of the pile group is affected by the group configuration. As a result, the pile group at

medium spacing is more sensitive to changes in the loading direction. Figure 2.6 compares the proportion of the total lateral load carried by each pile at 0:2D lateral displacement in the four tests.

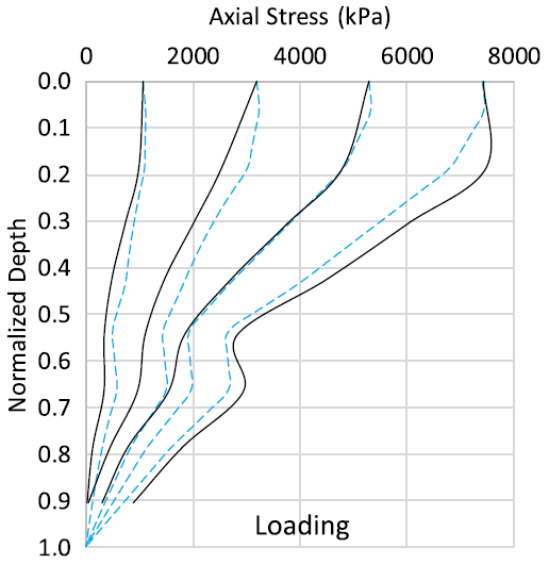

Figure 2.5 Axial stress along the length of the pile during loading (solid and dashed lines stand for test and model, respectively) (Dias & Bezuijen, 2018).

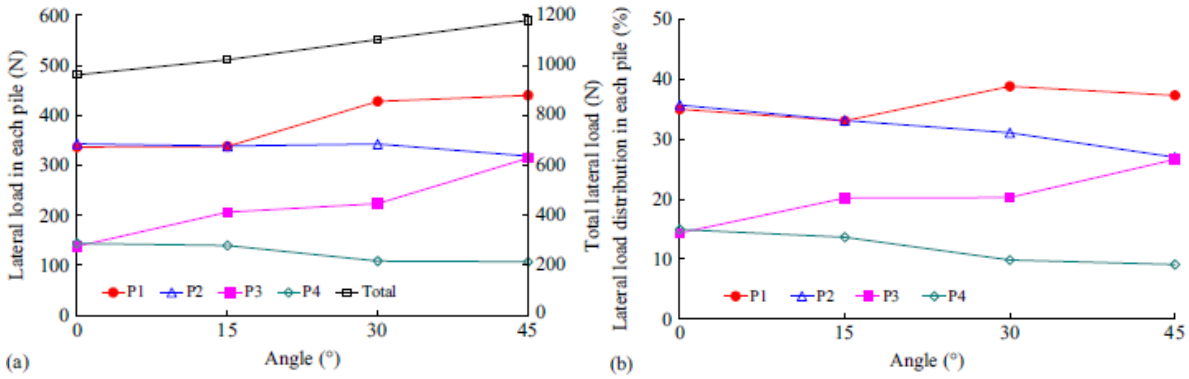

Figure 2.6 Influence of the loading direction on the response corresponding to the deflection of 0:2D for the 2 × 2 pile group at 5D × 5D spacing: (a) lateral load; (b) lateral load distribution (Su & Zhou, 2015).

2.6 STEEL PILES

Basack and Nimbalkar (2018) carried out small-scale laboratory tests with steel-pile groups in a remolded soft clay and sand layers. The test setup included static and cyclic loading devices, large-scale confining mold, central driving unit, and other peripheral devices. The cylindrical steel confining mold was utilized for retaining the compacted test bed of soft clay or layered soil. The mold had an internal diameter of 400 mm and an overall height of 650 mm. The layered soil comprised an upper layer of medium dense sand overlaying a soft clay bed. Experiments were carried out using instrumented and non-instrumented pile groups (2×2), with each steel-pipe pile having a 20-mm outer diameter, 5-mm thickness, and 500-mm overall length (depth of embedment = 400mm with length-to diameter ratio of 20). Two-dimensional (2D) plane-strain FE (2D FE) analysis was carried out using PLAXIS 2D Dynamic 2015. Embedded piles in PLAXIS 2D Dynamic 2015 were composed of beam (3-node line) elements. Based on the hyperbolic and parabolic patterns for lateral and vertical post-cyclic loadings, the load-displacement response was curvilinear. The average deviation between the test data and FEM results was reported to be approximately 5 to 10%. The post-cyclic load-displacement responses were found to degrade as the number of load cycles increased. The proposed 2D FE model was found to yield results close to the experimental data (Figure 2.7).

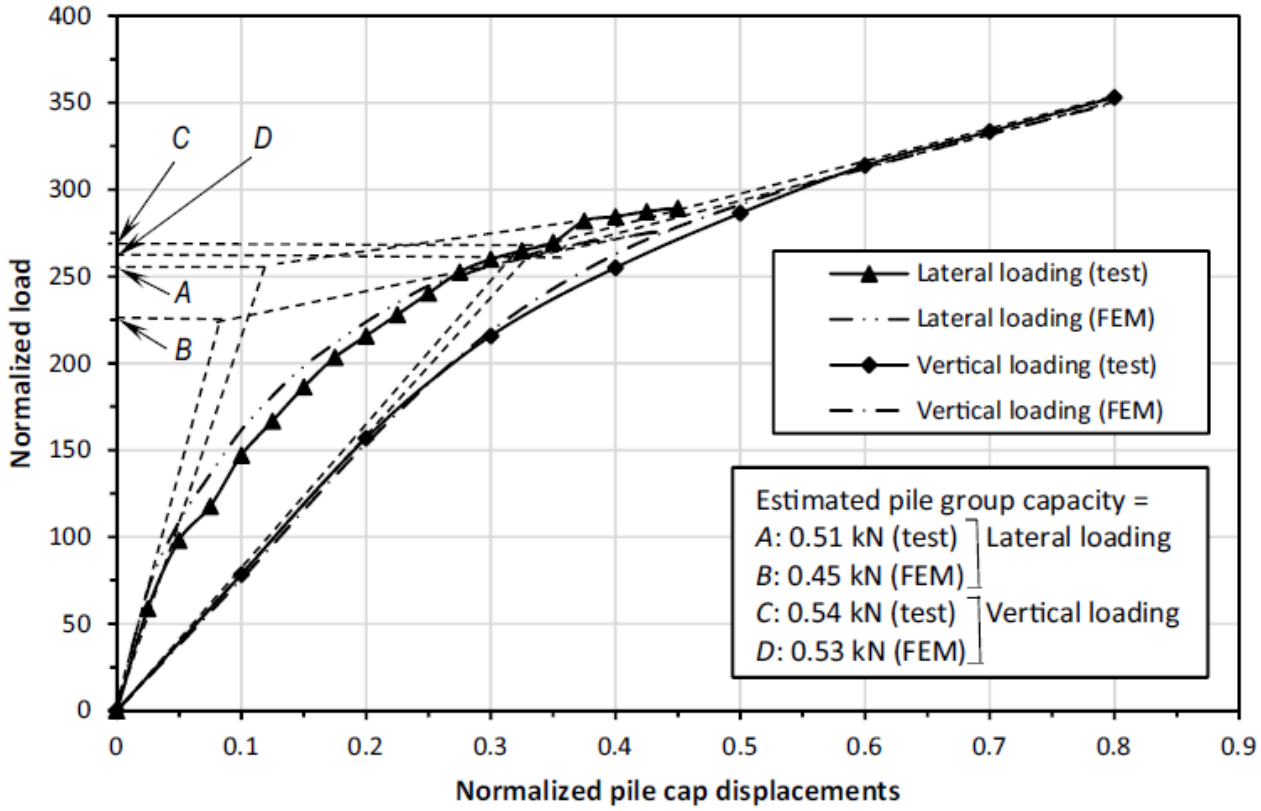

Figure 2.7 Estimation of the ultimate capacities of the pile group tested by Basack et al. (Basack & Nimbalkar, 2018).

Bhowmik et al. (2016) investigated the dynamic pile response under vertical load experimentally and numerically using Abaqus commercial software. The small-scale experimental data was used to verify and calibrate the model parameters. The resonant amplitude of the pile foundation increases and the resonant frequency decreases with the increase in excitation moment. The slippage between the pile and soil during vibration results in stiffness reduction of the pile-soil system. The maximum slippage between the pile and soil occurs close to the ground surface while the slippage decreases parabolically along the depth as shown in the Figure 2.8.

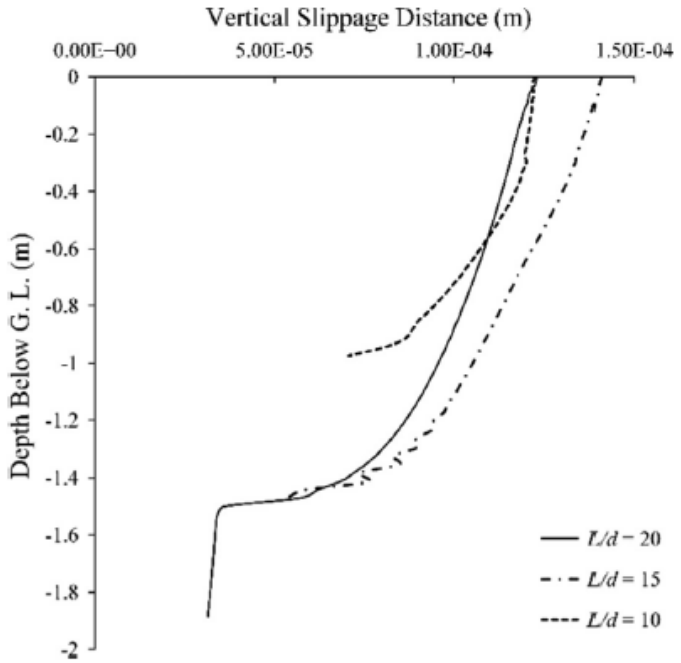

Figure 2.8 Maximum vertical slippage of steel pile surface along the length of the pile (Bhowmik et al., 2016).

Kim and Jeong (2011) proposed a 3D finite element (FE) model to simulate the behavior of a single pile under lateral loads in clay using PLAXIS 3D Foundation (Brinkgreve et al., 2007). Figure 2.9 shows the typical 3D FE mesh used to analyse a pile subjected to lateral loads. The width and height of model boundaries were 11 times the pile diameter (D) and 1.7 times the pile length (L), respectively. The aforementioned dimensions were considered satisfactory to eliminate the influence of boundary effects on the pile performance (Wallace et al., 2002). The mesh consisted of 17,500 nodes with the configuration of 15-node wedge elements and the outer boundary of the soil was fixed against displacements. To verify the FE model, the lateral load test results at Incheon site were employed to test the 3D FE model predictions. The comparison of the p–y curves from model and experiment along with models proposed by Matlock (1970) and O'Neil (1984) is presented in Figure 2.10.

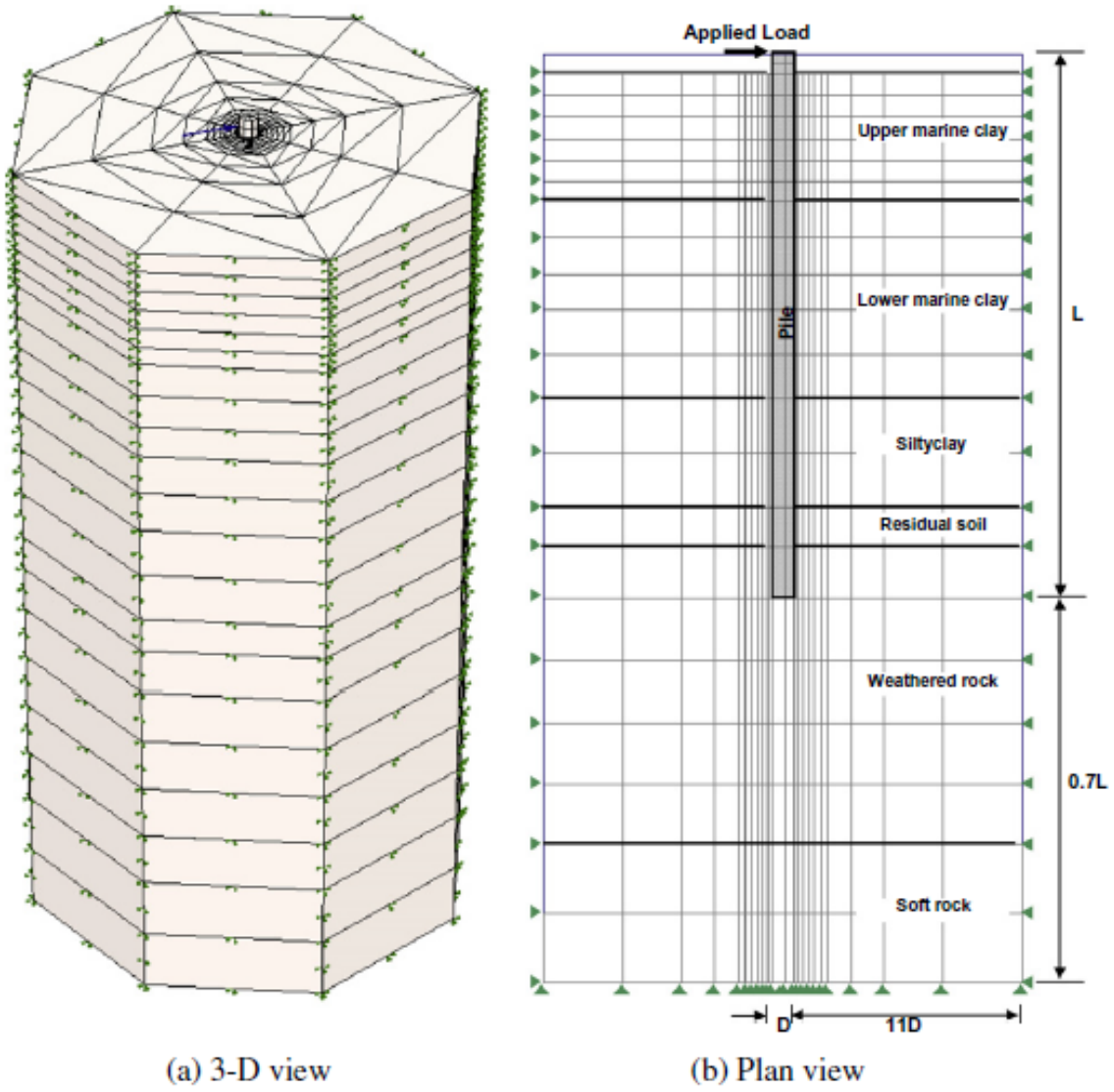

Figure 2.9 Schematic presentation of generated mesh for FE analysis of a single pile under lateral loads in clay (Kim & Jeong, 2011)

Tamura et al. (2012) investigated the effect of existing piles on new pile installation with cyclic lateral-loading centrifuge tests at the center of 2×2 existing pile in addition to the two-dimensional (2D) FEM analyses of the horizontal cross sections. Based on the results, adding a new pile to an existing pile group results in a slight increase in the lateral resistance of the corresponding pile. Furthermore, add a pile to pile group increases the horizontal reaction of the each pile near the soil surface while decreases the horizontal reaction near the tip of the pile.

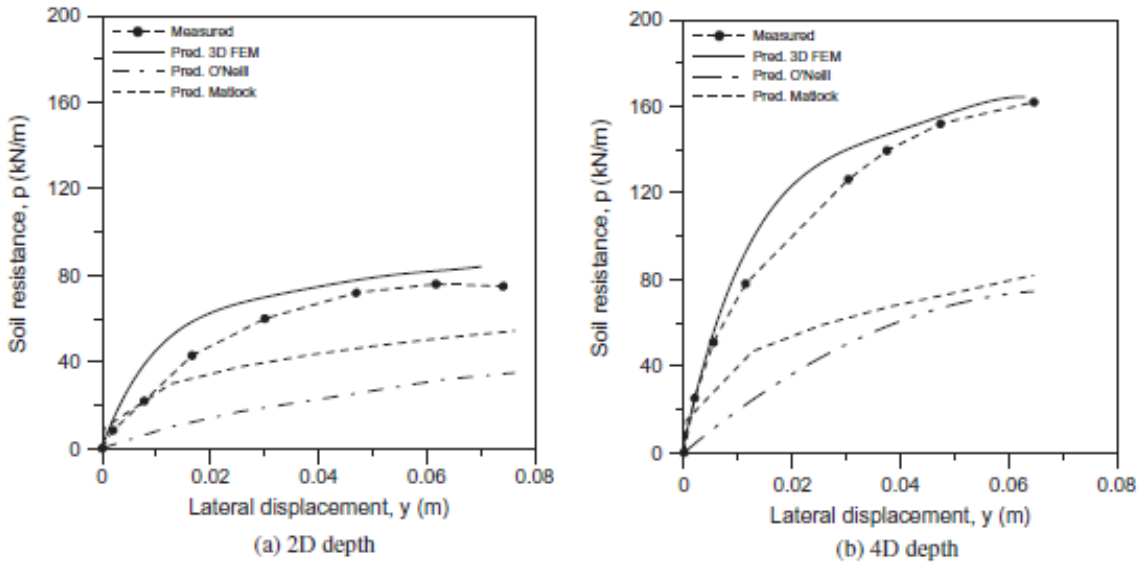

Figure 2.10 Comparison of p–y curves for steel pile: (a) 2D depth; (b) 4D depth (Kim & Jeong, 2011).

2.7 PILE INSTALLATION

Upon installation of a pile, the soil surrounding the pile is heavily distorted. Thus, the installation phase is generally not directly modeled in the FE analysis. Dijkstra et al. (2011) modeled the installation phase of a displacement pile using two numerical methods. In the first approach, the pile was considered to be fixed, while the soil moves along the pile similar to procedure provided by Berg et al. (1996; 1994). In this approach, the entire pile installation phase is considered a non-stationary flow of soil, as not all material has passed through the entire domain. At the end of pile installation, a stationary phase is reached, and the calculated stresses and strains are numerically correct. This modelling approach requires somewhat unrealistic boundary conditions and requires that the results for the pile installation are for a non-stationary phase of the calculation, while formally only the values at the stationary full penetration phase are reliable. Figure 2.11 shows a schematic configuration of the test setup for fixed and moving pile.

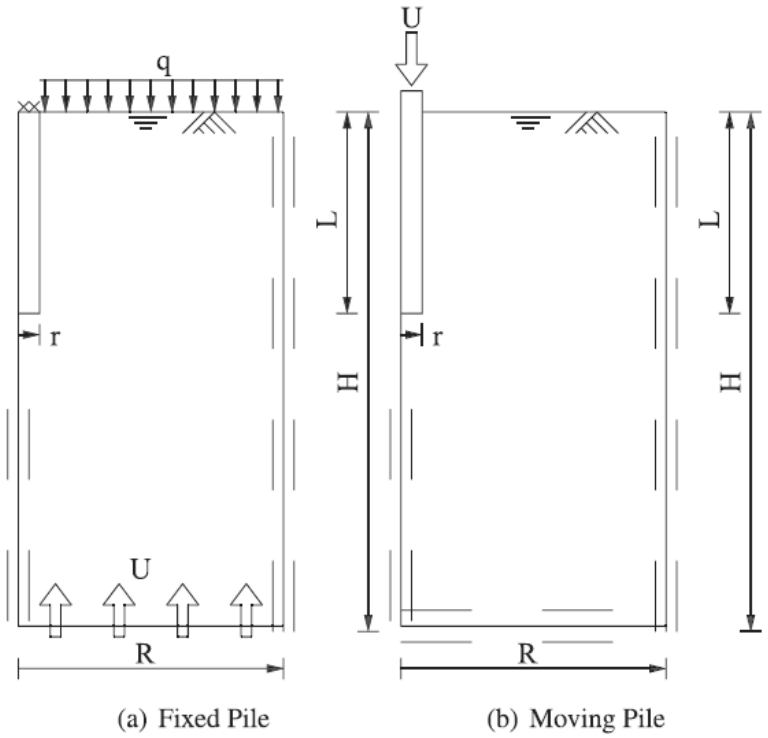

Figure 2.11 Geometry and boundary conditions for the two modelling approaches of the centrifuge test (Dijkstra et al., 2011).

To overcome the mentioned limitations, a second modelling approach was introduced by Dijkstra et al. (2011). In the new approach, the initial conditions are set at soil surface with zero stress level, increasing linearly with depth. Moreover, the stepwise penetration of the pile into the soil was achieved by using gravity loading stages. This approach updates the geometry of the problem domain and keeps updating the convective terms in a fixed mesh. The results were compared with experimental data from centrifuge tests. Although both models show the porosity change near the pile shaft and development of large effective vertical stress below the pile base, there were differences in the experimental results especially the stiffness response during pile installation. By comparing the calculated and measured values of the effective vertical stress below the pile base, as well as the porosity change near the pile shaft, large differences were observed for both the fixed and moving pile approaches. In particular, the stiffness during pile installation is difficult

to model. The moving pile approach is not in good accordance with the centrifuge test data, but an acceptable agreement with experimental penetration tests was observed near the surface level. The stress distribution of loose, medium dense and dense soil is shown in Figures 2.12 and 2.13 for fixed and moving pile. Based on a study conducted by Russo (2016), the installation procedure has less significant effect on piles under lateral loading with respect to those under axial loading. The load–deflection relationship is markedly nonlinear from the early stages of loading while the relationship between the applied head load and the observed maximum bending moments is approximately linear up to the corresponding displacement to the failure.

Zarrabi and Eslami (2016) studied the construction effects on the pile performance by using the frustum confining vessel of Amirkabir University of Technology (FCV-AUT) as shown in Figure 2.14. Six different installation methods for pile were investigated including jacking, drilling and grouting, driving, screwing, drilling and placing, and postgrouting. Up to 30 axial compressive and tensile load tests were carried out on different piles embedded in Babolsar sand, from the northern coast of Iran, with relative densities of 45% to 50% by using FCV-AUT instrument. Experimental results showed that among different pile installation methods, jacked and precast-in-place piles had the greatest and lowest axial strength, respectively (Figure 2.15). Moreover, the performance results of the different pile types in the experiment indicate that the axial bearing capacity of piles can be increased by using a cost-effective installation method. These modifications can lead to a reduction in the number and size of piles, and consequently result in cost-effective construction and time requirements.

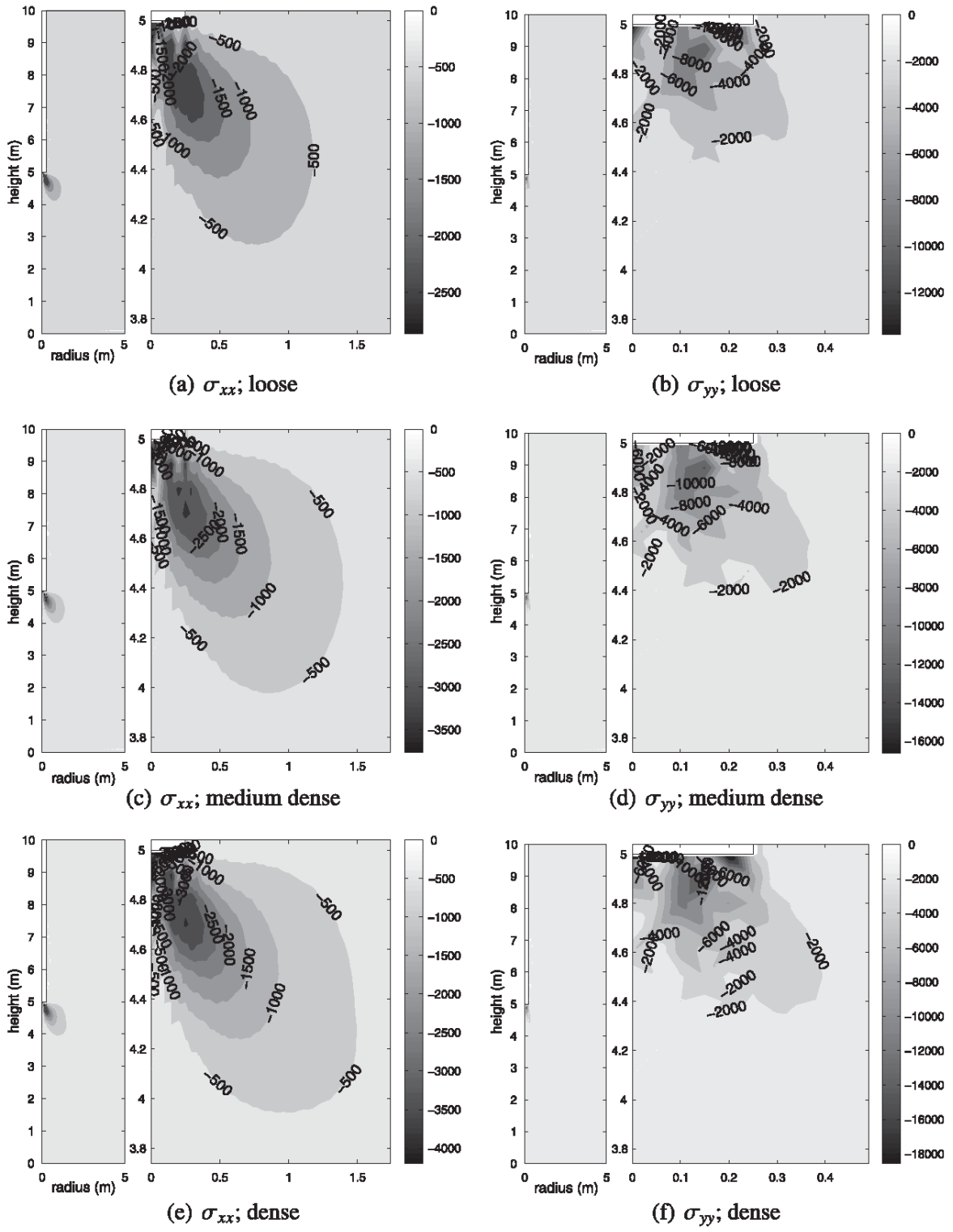

Figure 2.12 Fixed pile; calculated horizontal and vertical effective stress distribution upon 5 m of pile installation for three different initial soil densities (Dijkstra et al., 2011).

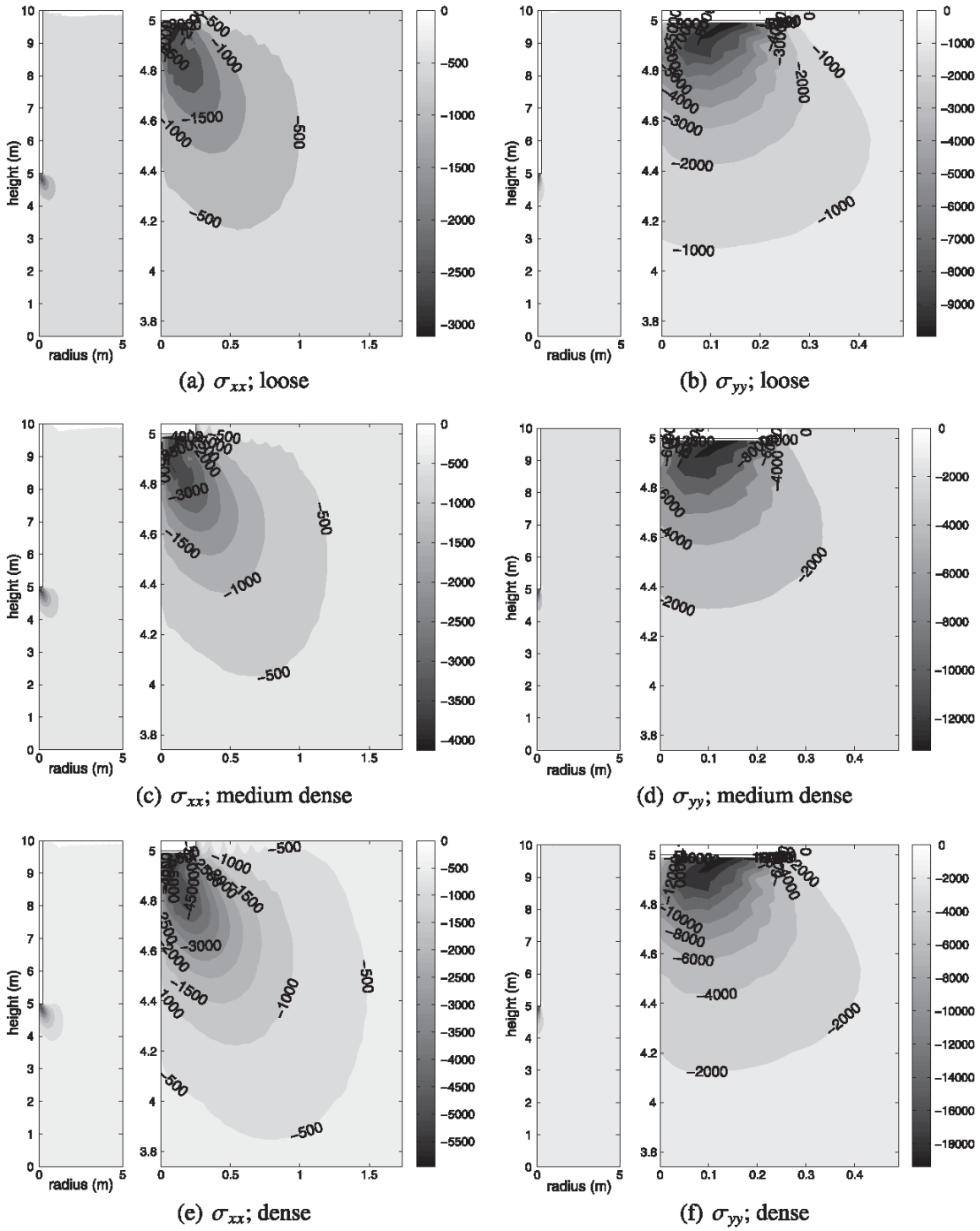

Figure 2.13 Moving pile; calculated horizontal and vertical effective stress distribution upon 5 m of pile installation for three different initial soil densities (Dijkstra et al., 2011).

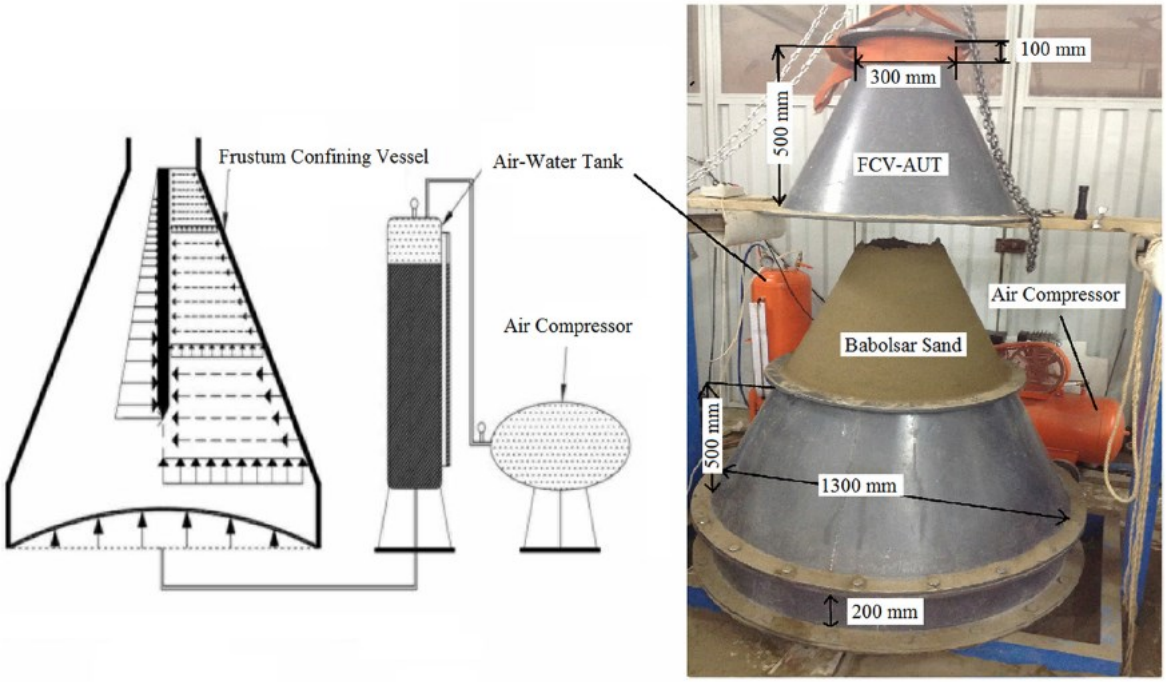

Figure 2.14 The FCV-AUT: (a) schematic diagram; (b) photograph (Zarrabi & Eslami, 2016).

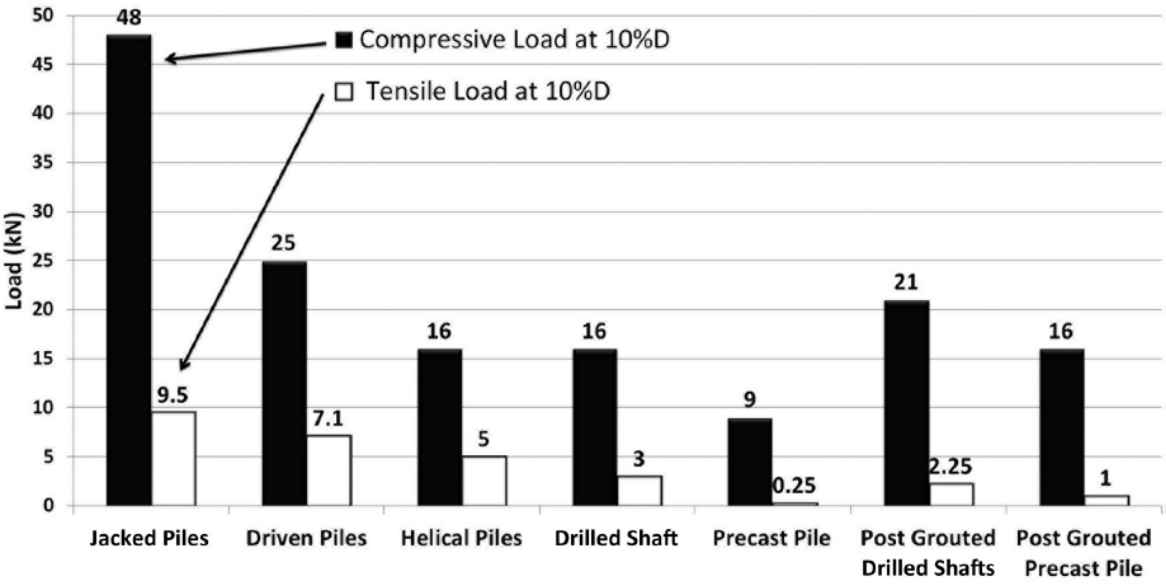

Figure 2.15 Compressive and tensile capacities of piles with different installation methods (Zarrabi & Eslami, 2016).

2.8 CONCRETE-FILLED FRP TUBES (CFFTS)

In 1996, Mirmiran and Shahawy (1996) initially proposed CFFTs as a mold for concrete, similar to conventional concrete-filled steel tubes. The results of uniaxial compression tests for CFFTs were compared with confinement models available in the literature (Mirmiran & Shahawy, 1997). Mirmiran et al. (2000) suggested a nonlinear finite analysis model (NFEM) with non-associative Drucker-Prager plasticity to predict stress-strain curves from test results. Fam and Rizkalla (2003; 2001a) investigated the behavior of CFFTs under uniaxial compression and under combined bending and axial loads. Mohamed and Masmoudi (2010a, 2010b) conducted a theoretical and experimental investigation of the flexural and axial behavior of concrete-filled FRP and steel tubes. Fam et al. (2005) studied glass FRP concrete-filled rectangular filament-wound tubes under axial and flexural loading. Ozbakkaloglu and Oehlers (2008) suggested a new method for making rectangular FRP tubes with unidirectional FRP sheets under axial compression. El-Nemr et al. (2016) studied the dynamic response of confined FRP tubes filled with concrete embedded in sandy soil. The results indicated that the fiber orientation and the elastic modulus of sand have a significant influence on the pile-displacement response under dynamic loading conditions.

Fam and Rizkalla (2001b) proposed an analytical model to predict the behavior of circular CFFTs by considering the biaxial state of stress in the FRP tube. Zhu et al. (2006) suggested a model for CFFTs embedded in a reinforced concrete footing, and conducted a parametric study of different column configurations. A case study was conducted by Pando et al. (2006) on CFFTs used in the foundation of a bridge on route 40 in Virginia, under axial and lateral loading. Nelson et al. (2008) explored the effect of moment connection of CFFTs to a concrete footing, and considered the bond strength and critical embedment length. Sadeghian and Fam (2010, 2011) provided an analytical model for moment connections of CFFT piles embedded directly in the footing under lateral and axial loads, based on deformation compatibility, equilibrium, and nonlinear concrete

stress-strain behavior. A parametric study was also conducted for parameters such as the diameter, thickness, and length of the composite pile. Furthermore, Sadeghian et al. (2011) conducted an experimental and numerical investigation of the moment connection of CFFTs with footings under monotonic and cyclic loading, and obtained critical stub lengths with different parameters.

2.9 MODELING

Hazzar et al. (2017) performed a 3D finite-difference (FD) analyses to evaluate the effects of vertical loads on the behavior of laterally loaded piles in layered soils corresponding to several configurations: homogeneous sandy or clayey soil layers, inhomogeneous clay layers, and multilayered strata. The validation of the proposed model was verified with two different published load tests, and then a parametric study was performed to investigate the effects of vertical loads on the lateral resistance and bending moment of the piles. Figure 2.16 shows the lateral load-deflection curves of piles in dense sand (Dr = 60%) with different percentages of vertical load (V). Numerical results showed that the lateral resistance of the pile did not vary considerably with vertical loads in a homogeneous sandy soil. On the other hand, applying vertical loads on a pile embedded in clayey soil was discovered to be detrimental to its lateral capacity leading to a non-conservative design.

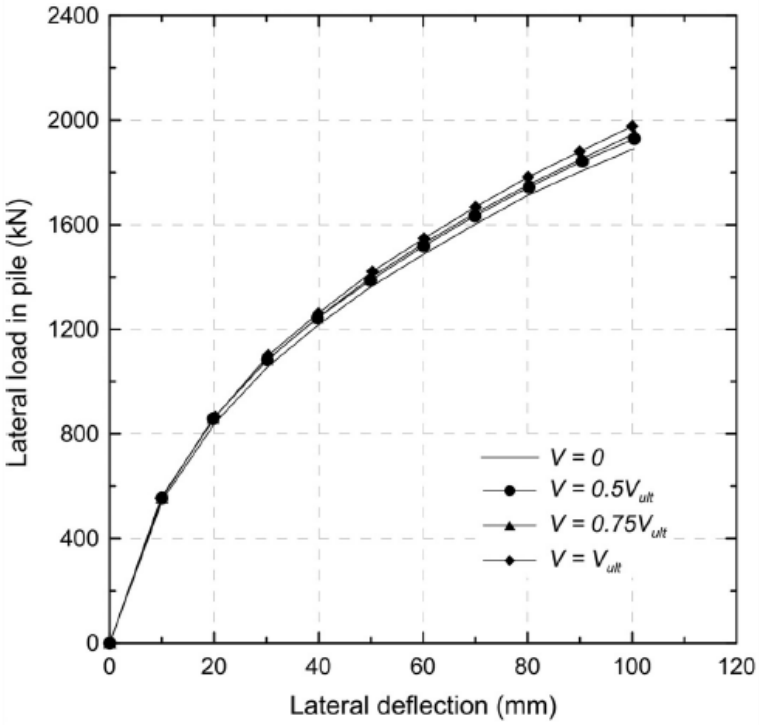

Figure 2.16 Lateral load-deflection curves of piles in dense sand (Hazzar et al., 2017).

Ladhane and Sawant (2016) developed a three-dimensional (3D) finite-element program for dynamic analysis of pile groups with interface elements to simulate the stress transfer between soil and pile under lateral load. Since flexural failure is predominant in piles and the failure of soil is controlled by its shear properties, eight-node and 20-node continuum elements were utilized to model the soil and pile, respectively. It is observed that the peak amplitudes of dynamic response reduce with an increase in pile spacing. A parametric study was conducted to investigate the effect of pile spacing, number of piles, arrangement of pile, and soil modulus on the behavior of pile group.

Based on the concept of the subgrade reaction theory, Zhang et al. (2013) proposed semi-analytical solutions using the power-series method to evaluate the response of a vertical pile with different cross sections and embedded in a multilayered soil system to support lateral loads at the head level. For the present method, the moduli of the lateral subgrade reaction were assumed to

be of constant depth for clay soil and of linearly increasing depth for sandy soil. The solution was verified by back-predicting responses of laterally loaded piles in two existing cases. Furthermore, four hypothetical cases for laterally loaded piles were considered in uniform and layered soil. By comparing results, it was noticed that the pile response was controlled by the subgrade soil stiffness at shallow depth of nearly 3–4 times the pile diameter.

2.10 DISTURBED STATE CONCEPT (DSC)

Desai (2001, 2015) proposed DSC damage model initially for granular materials such as sand and clay to model their corresponding post-peak behavior. Toufigh et al. (2016) investigated the behavior of polymer concrete under uniaxial compression test by using DSC and hierarchical single surface (HISS) plasticity model. HISS is a single-surface failure criterion meaning that it has no singularity point, which results in a more convenient yield surface with respect to other conventional models. In 2017, Toufigh et al. (2017) studied the elastoplastic behavior of polymer concrete as well as ordinary concrete under triaxial compression loading by using the NFEA along with the DSC damage model and the HISS failure criterion. Based on the results, the modeling results were in good agreement with experimental data meaning that the model is applicable to polymer concrete as well as ordinary concrete.

2.11 RESEARCH GAPS

Numerical simulation of test on piles often leads to errors and inaccuracies due to essentially the difficulty of taking account of installation effects and reproduce soil structure interface behavior. The application of fiber-reinforced plastics (FRP) in soil foundation has been mostly focused on FRP-wrapped piles. Using FRP as a formwork for the concrete piles results in: (a) reducing construction costs since no external molds are needed for pile installation, and (b) reducing long-term maintenance costs due to the fact that FRP laminate provides protection for concrete against

corrosive materials in the surrounding soil.

Although several studies have been conducted on the structural behavior of regular concrete piles and CFFT columns in the literature (Mirmiran & Shahawy, 1996, 1997; Mirmiran et al., 2000; Ozbakkaloglu, 2013), the lateral behavior of CFFT piles was not previously investigated numerically by using disturbed state concept (DSC). The interaction of concrete, FRP and soil is of great importance in geotechnical applications since it affects the pile load-bearing capacity as well as the soil stresses along the pile depth. Moreover, the application of FRP laminates in new structures as well as repair and rehabilitation of existing foundations requires a numerical modeling on the CFFT piles. It should be noted that the behavior of CFFT piles is more complex than that of conventional columns due to interface with the surrounding soil.

CHAPTER 3 NONLINEAR FINITE ELEMENT ANALYSIS

3.1 INTRODUCTION

To model the mechanical behavior of composite piles, a numerical model was developed using MATLAB software using nonlinear finite element analysis (NFEA). The geometrical and material nonlinearity was considered in the developed model in the form of large deformation and Mohr-Coulomb failure criterion. The details of the developed nonlinear finite element model based on large deformation and Mohr-Coulomb failure criterion procedure has been discussed in this section.

3.2 FAILURE CRITERIA

In order to define the elastoplastic behavior of a material, it is important to determine the failure initiation and damage evolution. The failure criterion defines the zone of elastic response, and it is corresponded to axial and lateral stresses. Therefore, the failure criterion can be expressed as follows (Zienkiewicz & Taylor, 2005):

$$F = F(\sigma_a, \sigma_l) \tag{3.1}$$

where F is the failure criterion function, and σ_a and σ_l are axial and lateral stresses at which the failure occurs, respectively. Generally, it can be represented by using six components of stress ($\underset{\sim}{\sigma}$) as follows:

$$F = F(\underset{\sim}{\sigma}) \tag{3.2}$$

With the assumption of isotropic material, F can be reduced to:

$$F = F(\sigma_1, \sigma_2, \sigma_3) \tag{3.3}$$

in which σ_1, σ_2 and σ_3 are the principal stresses. The yield function is typically defined by using the invariant stress tensor including J_1, J_2 and J_3 derived from the total stress tensor, as follows:

$$F = F(J_1, J_2, J_3) \tag{3.4}$$

Since the volumetric components of these stresses are not included in all plasticity models, they are usually defined by deviatoric components of J_2 and J_3 stresses indicated by J_{2D} and J_{3D}:

$$F = F(J_1, J_{2D}, J_{3D}) \tag{3.5}$$

where:

$$J_1 = \sigma_{ii}; \quad J_2 = \frac{1}{2}\sigma_{ji}\sigma_{ij} = \frac{1}{2}tr(\underset{\sim}{\sigma}^2) \quad J_3 = \frac{1}{3}tr(\underset{\sim}{\sigma}^3)$$

$$J_{2D} = \frac{1}{2}S_{ji}S_{ij}; \quad J_{3D} = \frac{1}{3}S_{ik}S_{km}S_{mi} \tag{3.6}$$

in which σ_{ij} and S_{ij} are the total and deviatoric stress tensor, respectively. The indices $i, j, k = 1, 2, 3$ represent the three components in the Cartesian coordinates for three-dimensional (3D) problems.

3.3 Mohr-Coulomb Plasticity Model

Mohr-Coulomb (MC) failure criterion can consider the friction of granular materials such as soil and concrete. The shape of MC in principal stress coordinates is a hexagonal cone as can be seen in Figure 3.1. One of the characteristics of this plasticity model is that it can result in different material strengths based on the loading path (Figure 3.2). Hence, it can provide better plasticity behavior for granular materials such as soil and concrete with respect to basic models such as

Tresca and Von Mises (Desai, 2001).

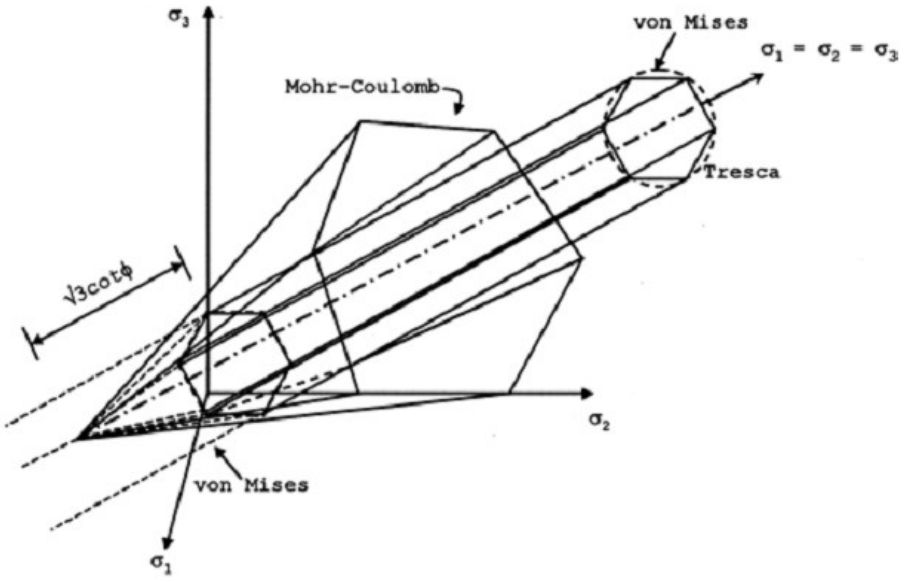

Figure 3.1 Comparison of Mohr-Coulomb, Tresca and Von Mises failure criterions in the principal stress coordinates (Desai, 2001).

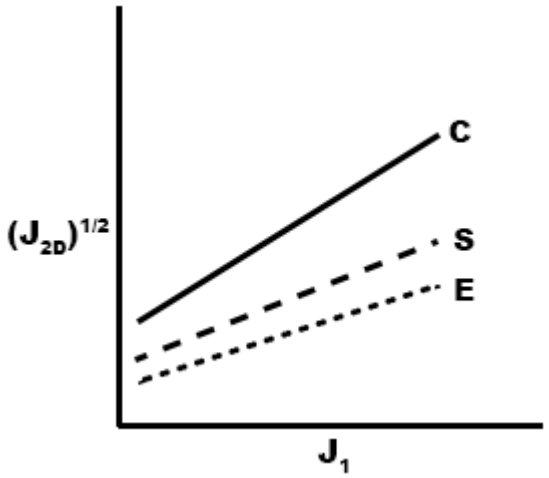

Figure 3.2 Schematic representation of Mohr-Coulomb (MC) failure envelope under different loading paths, where C: compression, E: extension or tension and S: shear (Desai, 2001).

The Mohr-Coulomb yielding function can be defined as (Khoei, 2005):

$$F = J_1 \sin\varphi + \sqrt{J_{2D}}\cos\theta - \frac{\sqrt{J_{2D}}}{3}\sin\varphi\sin\theta - c\cos\varphi = 0 \tag{3.7}$$

where c and φ are cohesion and internal friction angle and θ can be written as:

$$\theta = \frac{1}{3}\sin^{-1}\left(-\frac{3\sqrt{3}}{2}\frac{J_{3D}}{J_{2D}^{3/2}}\right) \tag{3.8}$$

which is in the range of $\frac{-\pi}{6} \le \theta \le \frac{+\pi}{6}$.

3.4 General Procedure of Elastoplastic Equations

The increment of total strain matrix of elastoplastic materials can be represented by two parts: elastic ($d\underset{\sim}{\varepsilon}^e$) and plastic ($d\underset{\sim}{\varepsilon}^p$) components as follows:

$$d\underset{\sim}{\varepsilon} = d\underset{\sim}{\varepsilon}^e + d\underset{\sim}{\varepsilon}^p \tag{3.9}$$

The increment of elastic strain can be written in terms of elastic strain increment as:

$$d\underset{\sim}{\sigma} = \underset{\sim}{C}^e d\underset{\sim}{\varepsilon}^e \tag{3.10}$$

where $\underset{\sim}{C}^e$ is the elastic stiffness matrix which depends on elastic modulus and Poisson's ratio. Based on the plasticity theory, the increment of plastic strain can be defined as (Khoei, 2010):

$$d\underset{\sim}{\varepsilon}^p = \lambda \frac{dQ}{\underset{\sim}{\sigma}} \tag{3.11}$$

in which, λ is a positive scalar parameter. By using compatibility condition of $dF = 0$ and partial derivate rule:

$$(\frac{dF}{d\underset{\sim}{\sigma}})^T \cdot d\underset{\sim}{\sigma} + \frac{dF}{} d\xi = 0 \tag{3.12}$$

where $d\xi$ can be written as:

$$\begin{aligned} d\xi &= [(d\underset{\sim}{\varepsilon}^p)^T \; d\underset{\sim}{\varepsilon}^p]^{1/2} \\ &= [\lambda(\frac{\partial Q}{\partial \underset{\sim}{\sigma}})^T \cdot \lambda(\frac{\partial Q}{\partial \underset{\sim}{\sigma}})]^{1/2} \\ &= \lambda[(\frac{\partial Q}{\partial \underset{\sim}{\sigma}})^T \cdot (\frac{\partial Q}{\partial \underset{\sim}{\sigma}})]^{1/2} \\ &= \lambda\gamma_f \end{aligned} \tag{3.13}$$

Therefore, Eq. 3.12 will be modified to:

$$(\frac{dF}{d\underset{\sim}{\sigma}})^T \cdot d\underset{\sim}{\sigma} + \frac{dF}{} \cdot \gamma_f = 0 \tag{3.14}$$

By substituting $d\underset{\sim}{\sigma}$ from Eq. 3.10 and $d\underset{\sim}{\varepsilon}^e$ from Eq. 3.9, the above equation will be modified to:

$$(\frac{dF}{d\underset{\sim}{\sigma}})^T \cdot \underset{\sim}{C}^e (d\underset{\sim}{\varepsilon} - d\underset{\sim}{\varepsilon}^p) + \frac{dF}{} \lambda \cdot \gamma_f = 0 \tag{3.15}$$

In addition, the plastic increment ($d\underset{\sim}{\varepsilon}^p$) can be plugged in from Eq. 3.11, which yields:

$$(\frac{dF}{d\underset{\sim}{\sigma}})^T \underset{\sim}{C}^e d\underset{\sim}{\varepsilon} - (\frac{dF}{} \underset{\sim}{C}^e \frac{dQ}{} + \frac{dF}{}) \cdot \lambda \cdot \gamma_f = 0 \tag{3.16}$$

As a result, the value of λ can be presented as:

$$\lambda = \frac{(\frac{dF}{d\underset{\sim}{\sigma}})^T \cdot \underset{\sim}{C}^e d\underset{\sim}{\varepsilon}}{(\frac{dF}{d\underset{\sim}{\sigma}})^T \underset{\sim}{C} \frac{dQ}{} + \frac{dF}{} \cdot \gamma_f} \tag{3.17}$$

Plugging the above equation into Eq. 3.10 yields:

$$d\underset{\sim}{\sigma} = \underset{\sim}{C}^{e}(d\underset{\sim}{\varepsilon} - d\underset{\sim}{\varepsilon}^{p})$$

$$= \left[\underset{\sim}{C}^{e} - \frac{\underset{\sim}{C}^{e} \dfrac{\partial Q}{\partial \sigma}\left(\dfrac{\partial F}{\partial \sigma}\right)^{T} \underset{\sim}{C}^{e}}{\left(\dfrac{\partial F}{\partial \sigma}\right)^{T} \underset{\sim}{C}^{e} \dfrac{\partial Q}{\partial \sigma} + \dfrac{\partial F}{\partial \kappa} \dfrac{\partial \kappa}{\partial \varepsilon^{p}} \dfrac{\partial Q}{\partial \sigma}} \right] d\underset{\sim}{\varepsilon} \tag{3.18}$$

The value in the brackets stands for elastoplastic stiffness matrix ($\underset{\sim}{C}^{ep}$).

3.5 DISTURBED STATE CONCEPT (DSC)

Based on the damage model proposed by Desai (2001), the material behavior can be divided into two parts including undisturbed and disturbed components. The disturbed behavior can be represented by the relative movement of material particles due to different factors such as micro cracks, slippage and rotation of material particles. Hence, the conventional concept of stress at an arbitrary point of the material $\sigma = P / A$ is not valid. The schematic representation of disturbed state concept (DSC) is shown in Figure 3.3; the material response is shown in relatively intact (RI) or elastically deformed behavior as well as fully adjusted (FA) or fully damaged behavior. The RI behavior depends on the type of material as well as elastic modulus and Poisson's ratio. For instance, RI response for a material with nonlinear elastic behavior can be defined as an elastic material without micro cracks. For elastoplastic behavior, however, it can be defined as elastic-perfectly plastic response. As a result, the plasticity will affect the computation load of RI behavior in the NFEA implementation.

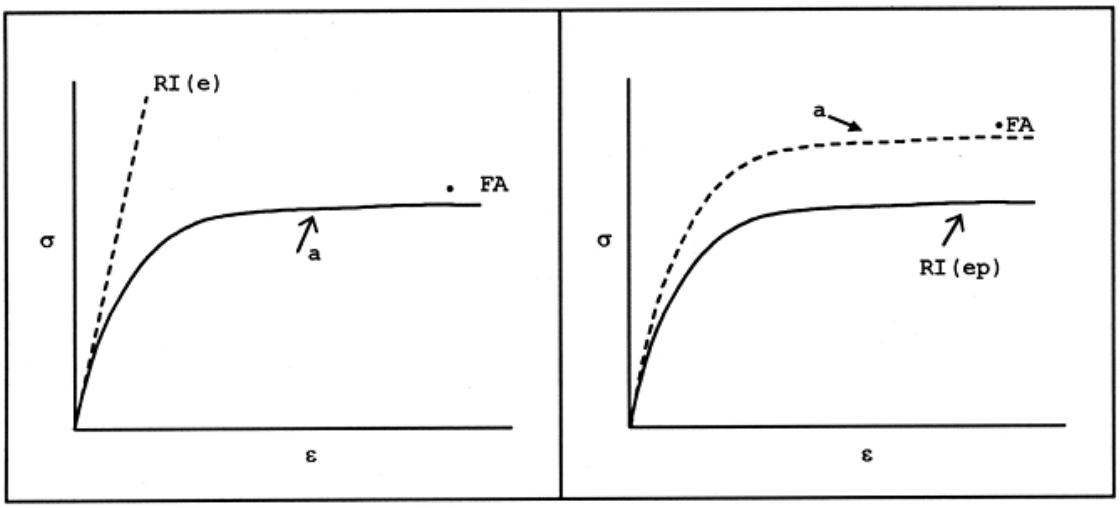

Figure 3.3 Schematic figures of DSC with elastic (e) and elastoplastic (ep) RI behaviors (Desai, 2001).

The actual FA response is practically not obtainable by laboratory testing. Hence, the residual strength of material obtained in the laboratory tests can be used for FA behavior.

3.6 THE DSC FORMULATION

Using equilibrium of forces in the material element composed of disturbed and undisturbed parts yields (Desai, 2001):

$$F^{\exp} = F^{i} + F^{c} \tag{3.19}$$

where $F^{\exp}$, F^{c} and F^{i} stand for the experimental force, RI force and FA force, respectively. By dividing both sides of Eq. 3.19 to total area of element (with unit height), the above equation can be written as:

$$\frac{F^{\exp}}{A} = \frac{F^{i}}{A^{i}} \cdot \frac{A^{i}}{A} + \frac{F^{c}}{A^{c}} \cdot \frac{A^{c}}{A} \tag{3.20}$$

in which A^{i} and A^{c} are the corresponding area to RI and FA parts, respectively as shown in

Figure 3.4. Therefore:

$$\sigma^{\exp} = \sigma^{i} \frac{A^{i}}{A} + \sigma^{c} \frac{A^{c}}{A} \tag{3.21}$$

where $\sigma^{\exp}$, σ^{i} and σ^{c} are stresses in experimental, RI and FA states, respectively. This equation in 3D can be written as (Desai, 2015):

$$\sigma_{ij}^{\exp} = (1-D)\sigma_{ij}^{i} + D\sigma_{ij}^{c} \tag{3.22}$$

where D is the disturbance function ($D = A^{c} / A$). Thus, the increment of disturbance function will be:

$$d\sigma_{ij}^{\exp} = (1-D)\,\mathrm{d}\,\sigma_{ij}^{i} + Dd\sigma_{ij}^{c} + dD(d\sigma_{ij}^{c} - \sigma_{ij}^{i}) \tag{3.23}$$

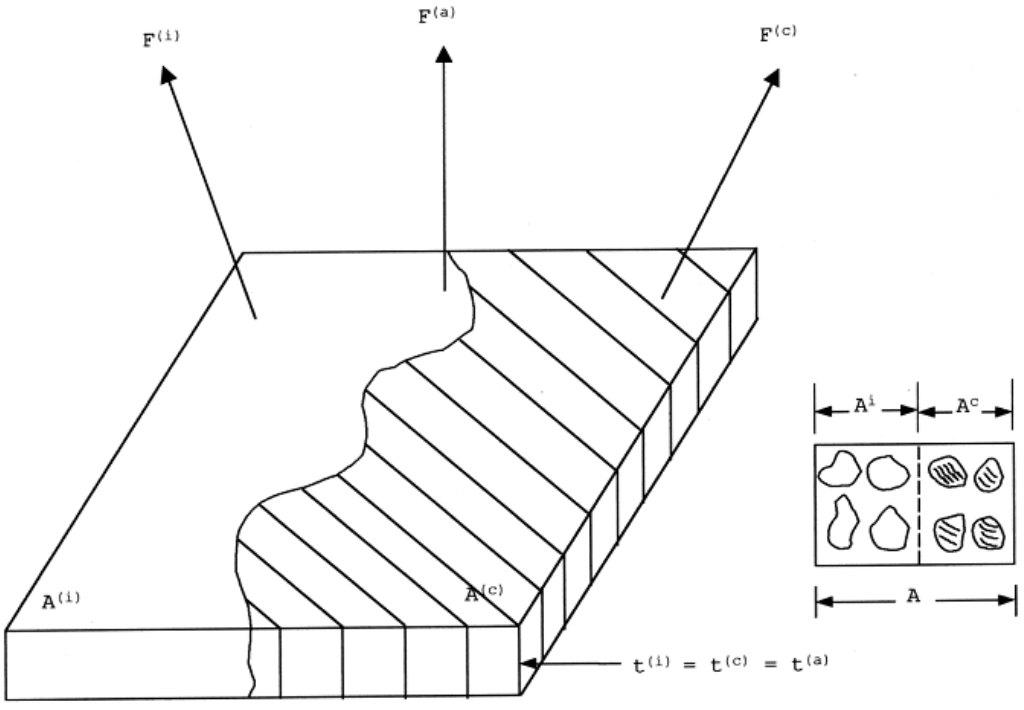

Figure 3.4 Schematic figure of material element composed of RI and FA parts (Desai, 2001).

The proposed model is based on the DSC damage model, which can be formulated as the decomposition of material behavior into its relatively intact (RI) and fully adjusted (FA) components. A schematic representation of the DSC damage model is shown in Figure 3.5, where the white and black areas represent the RI and FA components, respectively. In its initial response, all of the material is RI, without any visible cracks. As applied loading increases, the FA response becomes more predominant, and the propagation of cracks results in entirely FA behavior at failure. According to the concept proposed by Desai (2001), the disturbance can be represented as:

$$D = D_u(1 - e^{-A\zeta_D^Z}) \tag{3.24}$$

where D_u is the ultimate value of the disturbance, and A and Z are material parameters, and ζ_D is the trajectory of deviatoric plastic strain:

$$\zeta_D = \int (dE_{ij}^p dE_{ij}^p)^{\frac{1}{2}} \tag{3.25}$$

where E_{ij} is the deviatoric strain tensor of the total strain tensor ε_{ij}. The disturbance of the stress-strain curve can be generally represented as:

$$D = \frac{\sigma^{RI} - \sigma^{exp}}{\sigma^{RI} - \sigma^{FA}} \tag{3.26}$$

where σ^{RI}, σ^{FA} and σ^{exp} represent relatively intact (RI), fully adjusted (FA) and experimental stresses, respectively. In the modeling procedure, the RI and FA states are correlated as a function of deviatoric plastic strain (see Figure 3.6). As shown in the graph, the disturbance increases as the cracks propagate in the specimens. Eqs. (1) and (3) represent two arbitrary points on the experimental curve, to find the A and Z parameters.

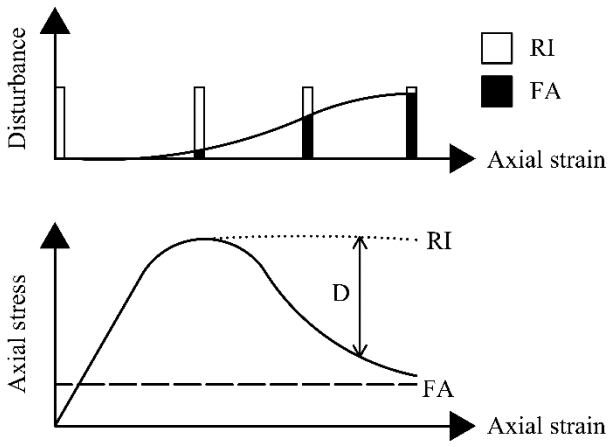

Figure 3.5 Schematic representation of DSC damage model based on the concept by Desai (2001)

The three parameters D_u, A, and Z are the disturbance parameters used to predict the mechanical behavior of the corresponding material in experimental or field tests. The residual strength and confining conditions control the FA behavior, whereas the elastic modulus and type of adhesive material affect the RI behavior. Once the disturbance parameters are defined for each specimen, stress increments can be obtained from the following equation (Desai, 2015):

$$d\sigma_{ij} = (1-D)C^{ep}_{ijkl}d\varepsilon_{kl} + \frac{D}{3}\delta_{ij}C^{ep}_{ppkl}d\varepsilon_{kl} - dD(\sigma^{RI}_{ij} - \sigma^{FA}_{ij}) \tag{3.27}$$

The disturbance value (D) equals zero in the pre-failure stage. Models that can be used to predict the RI response of the material range from simple mathematical models to constitutive models such as the Mohr-Coulomb failure criterion. In this research, NFEA and the Mohr-Coulomb failure criterion are used to predict the RI response.

3.7 MODELING PROCEDURE

The flowchart of modeling procedure has been shown in Figure 3.6. In the first step, the

parameters of the generated model were defined in six sections: a) generating a mesh for the geometry of the pile, FRP tube and surrounding soil; b) defining the nodal freedom of the problem which was fixed nodes for the boundaries of soil except the top surface as well as the node corresponding to prescribed lateral load applied at the top of composite pile; c) applying the lateral load at the top of CFFT pile; d) the number of loading steps was chosen to be 100 steps; e) defining the elastic parameters and stiffness matrix; f) the Gaussian points were also defined in this phase. In the next phase, the stress, strain, displacement and forces were initialized with zero values.

In the third phase of modeling, the first lateral loading increment was applied to the composite pile. The failure of each of eight Gaussian's point was checked: if it failed the elastic matrix was corrected by elastoplastic matrix, otherwise plastic correction was not needed. The large deformation procedure was formulated in several iterations to meet the required error tolerance defined which was 0.01 for relative displacements. This loop of loading increments was continued until reaching the last step. Afterwards, the DSC damage model was applied to consider the softening behavior of granular material including concrete and soil. The discussion of the elastoplastic formulation used in each loading increment has been discussed in the following sections.

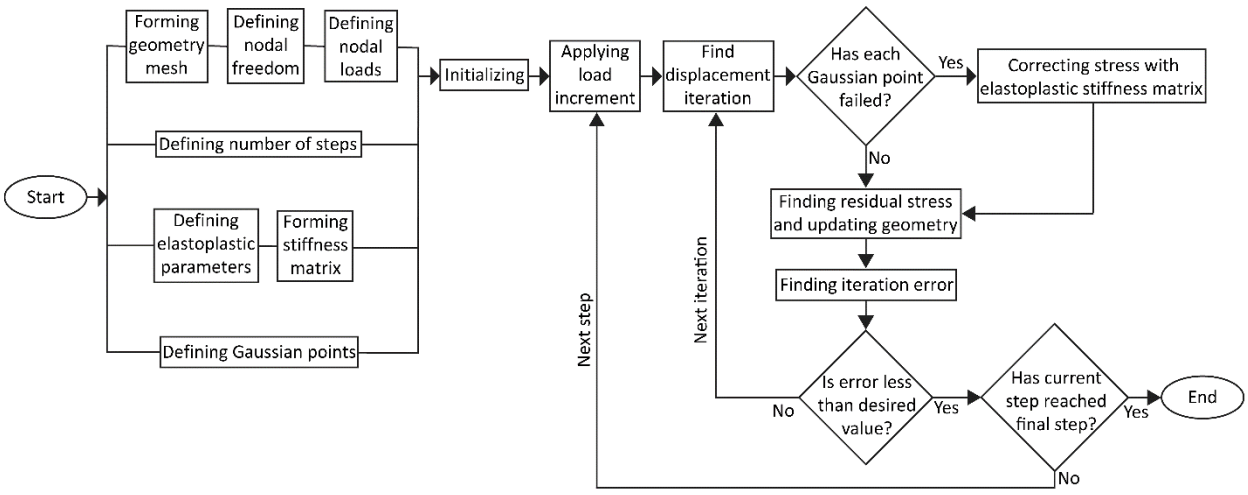

Figure 3.6 Flowchart of the proposed model for CFFT and normal concrete piles under lateral loading.

3.7.1 BASIC EQUATIONS OF CONTINUUM DEFORMATION

This second-order model can be used to simulate the behavior of sands and gravel as well as softer types of soil such as clays and silts. The static equilibrium of a continuum can be formulated as (Zienkiewicz & Taylor, 2005):

$$\mathbf{L}^{\mathrm{T}}\boldsymbol{\sigma}+\mathbf{b}=\mathbf{0} \tag{3.28}$$

This equation relates the spatial derivatives of the six stress components, assembled in the vector $\boldsymbol{\sigma}$, to the three components of the body forces, assembled in vector $\mathbf{b}$. $\mathbf{L}^{\mathrm{T}}$ is the transpose of a differential operator, defined as:

$$\mathbf{L}^{\mathrm{T}}=\begin{bmatrix} \frac{\partial}{\partial x} & 0 & 0 & \frac{\partial}{\partial y} & 0 & \frac{\partial}{\partial z} \\ 0 & \frac{\partial}{\partial y} & 0 & \frac{\partial}{\partial x} & \frac{\partial}{\partial z} & 0 \\ 0 & 0 & \frac{\partial}{\partial z} & 0 & \frac{\partial}{\partial y} & \frac{\partial}{\partial x} \end{bmatrix} \tag{3.29}$$

In addition to the equilibrium equation, the kinematic relation can be formulated as $\boldsymbol{\varepsilon} = \mathbf{L}\mathbf{u}$ which expresses the six strain components, assembled in vector $\boldsymbol{\varepsilon}$, as the spatial derivatives of the three displacement components, assembled in vector $\mathbf{u}$, using the previously defined differential operator **L**. The link between Eqs. 3.28 and kinematic relation is formed by a constitutive relation representing the material behavior. The equilibrium equation is reformulated in a weak form according to Galerkin's variation principle:

$$\int \boldsymbol{\delta}\mathbf{u}^{\mathrm{T}}(\mathbf{L}^{\mathrm{T}}\boldsymbol{\sigma} + \mathbf{b})\mathbf{dV} = 0 \tag{3.30}$$

In this formulation, $\boldsymbol{\delta}\mathbf{u}$ represents a kinematically admissible variation of displacements. Applying Green's theorem for partial integration to the first term in Eq. 3.30 leads to:

$$\int \boldsymbol{\delta\varepsilon}^{\mathrm{T}}\boldsymbol{\sigma}\mathbf{dV} = \int \boldsymbol{\delta}\mathbf{u}^{\mathrm{T}}\mathbf{b}\mathbf{dV} + \int \boldsymbol{\delta}\mathbf{u}^{\mathrm{T}}\mathbf{t}\mathbf{dS} \tag{3.31}$$

This introduces a boundary integral in which the boundary traction appears. The three components of the boundary traction are assembled in the vector t. Eq. 3.31 is referred to as the virtual work equation. The development of the stress state $\boldsymbol{\sigma}$ can be regarded as an incremental process:

$$\boldsymbol{\sigma}^{i} = \boldsymbol{\sigma}^{i-1} + \boldsymbol{\Delta\sigma} \tag{3.32}$$

In this relation, $\boldsymbol{\sigma}^{i}$ represents the actual state of stress which is unknown and $\boldsymbol{\sigma}^{i-1}$ represents the previous state of stress which is known and the stress increments are represented by $\boldsymbol{\Delta\sigma}$. If Eq. 3.31 is considered for the actual state i, the unknown stresses $\boldsymbol{\sigma}^{i}$ can be eliminated using Eq. 3.32:

$$\int \boldsymbol{\delta\varepsilon}^{\mathrm{T}}\boldsymbol{\Delta\sigma}\mathbf{dV} = \int \boldsymbol{\delta}\mathbf{u}^{\mathrm{T}}\mathbf{b}^{\mathrm{i}}\mathbf{dV} + \int \boldsymbol{\delta}\mathbf{u}^{\mathrm{T}}\mathbf{t}^{\mathrm{i}}\mathbf{dS} - \int \boldsymbol{\delta\varepsilon}^{\mathrm{T}}\boldsymbol{\sigma}^{\mathrm{i-1}}\mathbf{dV} \tag{3.33}$$

3.7.2 FINITE ELEMENT DISCRETIZATION

According to the finite element method a continuum is divided into a number of (volume) elements. Each element consists of a number of nodes. Each node has a number of degrees of freedom that correspond to discrete values of the unknowns in the boundary-value problem to be solved. In the case of deformation theory, the degrees of freedom correspond to the displacement components. The displacement field **u** is obtained from the discrete nodal values in a vector **v** using shape functions assembled in matrix **N**:

$$\mathbf{u} = \mathbf{N}\mathbf{v} \tag{3.34}$$

The interpolation functions in matrix N are often denoted as shape functions. Substitution of Eq. 3.34 in the kinematic relation gives:

$$\boldsymbol{\varepsilon} = \mathbf{L}\mathbf{N}\mathbf{v} = \mathbf{B}\mathbf{v} \tag{3.35}$$

In this relation B is the strain interpolation matrix, which contains the spatial derivatives of the interpolation functions. Eqs. 3.34 and 3.35 can be used in variational, incremental and rate form. Eq. 3.33 can now be reformulated in discretized form as:

$$\int (\mathbf{B}\delta\mathbf{v})^T \Delta\boldsymbol{\sigma} dV = \int (\mathbf{N}\delta\mathbf{v})^T \mathbf{b}^i dV + \int (\mathbf{N}\delta\mathbf{v})^T \mathbf{t}^i dS - \int (\mathbf{B}\delta\mathbf{v})^T \boldsymbol{\sigma}^{i-1} dV \tag{3.36}$$

The discrete displacements can be placed outside the integral and canceled out for any kinematically admissible displacement variation $\delta\mathbf{v}^T$ leading to the following equation:

$$\int \mathbf{B}^T \Delta\boldsymbol{\sigma} dV = \int \mathbf{N}^T \mathbf{b}^i dV + \int \mathbf{N}^T \mathbf{t}^i dS - \int \mathbf{B}^T \boldsymbol{\sigma}^{i-1} dV \tag{3.37}$$

The above equation is the elaborated equilibrium condition in discretized form. The first term on the right-hand side together with the second term represent the current external force vector and

the last term represents the internal reaction vector from the previous step. A difference between the external force vector and the internal reaction vector should be balanced by a stress increment ($\boldsymbol{\Delta\sigma}$).

The stress-strain increments have a nonlinear relation in most applications. As a result, strain increments can not be generally calculated directly, and global iterative procedures are required to satisfy the equilibrium condition Eq. 3.37 for all material points.

3.7.3 IMPLICIT INTEGRATION OF DIFFERENTIAL PLASTICITY MODEL

The stress increments are obtained by integration of the stress rates according to Eq. 3.32. For differential plasticity models the stress increments can generally be written as:

$$\boldsymbol{\Delta\sigma} = \mathbf{C}^{\mathbf{e}}(\boldsymbol{\Delta\varepsilon} - \boldsymbol{\Delta\varepsilon}^{\mathbf{p}}) \tag{3.38}$$

In this relation, $\mathbf{C}^{\mathbf{e}}$ represents the elastic material matrix for the current stress increment. The strain increments $\boldsymbol{\Delta\varepsilon}$ are obtained from the displacement increments $\boldsymbol{\Delta v}$ using the strain interpolation matrix **B**, similar to Eq. 3.37. For elastic material behavior, the plastic strain increment $\boldsymbol{\varepsilon}^{\mathbf{p}}$ is zero. For plastic material behavior, the plastic strain increment can be written, according to Vermeer (1979), as:

$$\boldsymbol{\Delta\varepsilon}^{\mathbf{p}} = \Delta\lambda\left[(1-\omega)\left(\frac{\partial g}{\partial \boldsymbol{\sigma}}\right)^{i-1} + \omega\left(\frac{\partial g}{\partial \boldsymbol{\sigma}}\right)^{i}\right] \tag{3.39}$$

In this equation, $\Delta\lambda$ is the increment of the plastic multiplier and ω is a parameter indicating the type of time integration. For $\omega = 0$ the integration is called explicit and for $\omega = 1$ the integration is called implicit. Vermeer (1979) has shown that the use of implicit integration ($\omega = 1$) has some major advantages, as it overcomes the requirement to update the stress to the yield surface in the

case of a transition from elastic to elastoplastic behavior. Moreover, it can be proven that implicit integration, under certain conditions, leads to a symmetric and positive differential matrix $\partial\boldsymbol{\varepsilon}/\partial\boldsymbol{\sigma}$, which has a positive influence on iterative procedures. Because of these major advantages, restriction was considered over other methods. Hence, the plastic strain for $\omega = 1$ can be written as:

$$\boldsymbol{\Delta\varepsilon}^{\mathbf{p}} = \Delta\lambda\left(\frac{\partial g}{\partial\boldsymbol{\sigma}}\right)^{i} \tag{3.40}$$

Substituting this equation in Eq. 3.38 and subsequently Eq. 3.32 yields:

$$\boldsymbol{\sigma}^{i} = \boldsymbol{\sigma}^{tr} - \Delta\lambda\mathbf{C}^{\mathbf{e}}\Delta\boldsymbol{\varepsilon} \tag{3.41}$$

In this relation, $\boldsymbol{\sigma}^{tr}$ is an auxiliary stress vector that referred to as the elastic stresses or trial stresses, which can be represented as:

$$\boldsymbol{\sigma}^{tr} = \boldsymbol{\sigma}^{i-1} + \mathbf{C}^{\mathbf{e}}\Delta\boldsymbol{\varepsilon} \tag{3.42}$$

The increment of the plastic multiplier $\Delta\lambda$ can be solved from the condition that the new stress state has to satisfy the yield condition:

$$f(\boldsymbol{\sigma}^{i}) = 0 \tag{3.43}$$

For perfectly-plastic and linear hardening models the increment of the plastic multiplier can be shown as:

$$\Delta\lambda = \frac{f(\boldsymbol{\sigma}^{tr})}{d+h} \tag{3.44}$$

where:

$$d = \left(\frac{\partial f}{\partial \boldsymbol{\sigma}}\right)^{\boldsymbol{\sigma}^{tr}} \mathbf{C}^{e} \left(\frac{\partial g}{\partial \boldsymbol{\sigma}}\right)^{i} \tag{3.45}$$

The symbol h denotes the hardening parameter, which is zero for perfectly-plastic models and constant for linear hardening models.

3.7.4 MATERIAL AND GEOMETRY NONLINEARITY

To satisfy the equilibrium conditions between internal and external forces, the norm of the following residual stress ($\boldsymbol{\psi}$) must approach zero through the required iterations (Khoei, 2005):

$$\boldsymbol{\psi} = \int_{V} \bar{\mathbf{B}}\boldsymbol{\sigma} \mathrm{d}_{V} - \mathbf{F} \tag{3.46}$$

where $\mathbf{F}$ represents the external force tensor, V represents the volume of the specimen, $\boldsymbol{\sigma}$ represents the Cauchy stress tensor, and $\bar{\mathbf{B}}$ represents the tensor for the increments of strain and displacement ($\Delta\boldsymbol{\varepsilon} = \bar{\mathbf{B}}\Delta\bar{\mathbf{u}}$). The shape functions used for numerical integration corresponding to the mapped hexahedron elements were defined as:

$$\begin{aligned}
N_1 &= \frac{1}{8}(1-\xi)(1-\eta)(1-\zeta) & N_5 &= \frac{1}{8}(1-\xi)(1-\eta)(1+\zeta) \\
N_2 &= \frac{1}{8}(1+\xi)(1-\eta)(1-\zeta) & N_6 &= \frac{1}{8}(1+\xi)(1-\eta)(1+\zeta) \\
N_3 &= \frac{1}{8}(1+\xi)(1+\eta)(1-\zeta) & N_7 &= \frac{1}{8}(1+\xi)(1+\eta)(1+\zeta) \\
N_4 &= \frac{1}{8}(1-\xi)(1+\eta)(1-\zeta) & N_8 &= \frac{1}{8}(1-\xi)(1+\eta)(1+\zeta)
\end{aligned} \tag{3.47}$$

where ξ, η and ζ are the unit coordinates for the mapped hexahedron element. To find the value of stress for each loading step, the increment of stresses can be expressed as:

$$\Delta\boldsymbol{\sigma}_{ij} = \mathbf{C}_{ijkl}\Delta\boldsymbol{\varepsilon}_{kl} \ \ (\mathrm{i},\ \mathrm{j},\ \mathrm{k},\ \mathrm{l} = 1,2,3) \tag{3.48}$$

where **C** is the stiffness matrix, which can be elastic ($\mathbf{C}^{e}$) or elastic-plastic ($\mathbf{C}^{ep}$), depending upon whether the corresponding Gaussian point has yielded or not. The indices *i, j, k* and *l* are tensor indices. The elastic-plastic stiffness matrix can be expressed as (Akhaveissy et al., 2009):

$$\mathbf{C}^{ep} = \mathbf{C}^{e} - \frac{\mathbf{C}^{e}\mathbf{n}\mathbf{n}^{T}\mathbf{C}^{e}}{H + \mathbf{n}^{T}\mathbf{C}^{e}\mathbf{n}} \tag{3.49}$$

where H is the hardening modulus, and **n** is the flow rule vector that shows the growth direction of the failure surface.

3.8 Model Limitations

- The FRP tube was assumed to be homogenous and isotropic.
- The initial soil stresses due to installation phase was assumed to be zero.
- The model cannot capture small deformations as opposed to large deformations.
- The effect of axial load on the lateral behavior of the pile was not considered.

CHAPTER 4 CALIBRATION AND PARAMTERIC STUDY

4.1 INTRODUCTION

The failure of bridge foundations exposed to corrosion in a marine environment can result in the collapse of the entire structure. Therefore, this issue is an important concern for civil engineers and governments in the design of stable infrastructures since the safety and durability of the bridge structures necessitates long-term maintenance costs. Replacing corroded piles can be difficult and expensive due to the fact that the bridge superstructure is relying on the foundation (Roddenberry et al., 2014). For this reason, highway agencies and researchers have begun to investigate the use of anti-corrosive materials and the viability of protecting bridge piles with composite materials such as fiber-reinforced polymer (FRP) composites, especially in the form of concrete-filled FRP tube (CFFT) piles (Fam et al., 2003).

It is important to consider the interaction of CFFTs and soil, since the behavior of underground piles is more complex than that of conventional columns. In the present research, a nonlinear finite element model is developed to predict the mechanical behavior of CFFT piles embedded in soil. The damage model and failure criterion used in the proposed model are based on the disturbed state concept (DSC) and the Mohr-Coulomb failure criterion, respectively. To verify the computational results, experimental data from precast CFFT piles used in the construction of a new bridge on route 40 in Virginia (Pando et al., 2006) were used to obtain the model parameters for different lateral loadings, from 48.9 to 120.1 kN. Moreover, a parametric study was carried out to determine the effects of the specimen length to diameter ratio, FRP tube thickness, concrete strength, and surrounding soil.

4.2 NUMERICAL MODELING

The two main structural components of CFFT piles are the concrete infill and the FRP tube. The relative stiffness of these two components controls the pile performance in relation to vertical and lateral loads. A numerical model based on the DSC damage model and the Mohr-Coulomb failure criterion is developed to predict the elastic-plastic behavior of CFFT piles under various lateral loading conditions, by using nonlinear finite element analysis in three dimensions. The interface of composite piles with the confining soil is also investigated in the proposed model.

4.2.1 PROPOSED MODEL

The mechanical behavior of CFFTs and concrete piles can be predicted by the proposed model. It should be noted that this model can also be used for CFFT columns, which are a special case of CFFT piles. The main factors addressed by the model are: (i) the contact problem associated with the interface of concrete, FRP laminate and soil, (ii) large deformations, considered in several increments and iterations, (iii) the modeling of plasticity by using a hierarchical single surface (HISS) failure criterion, and (iv) the softening effect of concrete in compression, based on the disturbed state concept.

Based on the schematic flowchart of the proposed model presented in Figure 3.6, the initial steps in developing the model involved defining the problem geometry, the number of steps, the elastoplastic parameters, and the Gaussian points for initial interpolation and final extrapolation of the stress and strain values. Nodal freedom and loads can be determined by generating a mesh of elements for finite element analysis (FEA).

A three-dimensional mesh of elements was generated for a cylindrical CFFT pile. A schematic representation of the generated mesh is shown in Figure 4.1. Total number of elements used for

soil, concrete and FRP tube were approximately 85,000, 12,500 and 750, respectively. As can be seen in the figure, the boundary conditions were considered by restraining the perpendicular displacement along the soil boundaries. It should be noted that the zoomed-in figure shows a more accurate representation of the mesh density used in the modeling. Each element was mapped onto a cubic element with unit dimensions as shown for an arbitrary element in Figure 4.2. For each element, the stresses were calculated for eight quadratic Gaussian points, by using values of $3^{-1/2}$ for the coordinates, with respect to the unit value in each direction (Zienkiewicz & Taylor, 2005). After the main calculations were performed, to extract the modeling results, the stress values were extrapolated by the same reverse procedure as for the element nodes. Thus, the mapped cubic elements with unit dimensions were utilized for the interpolation and extrapolation of stress values.

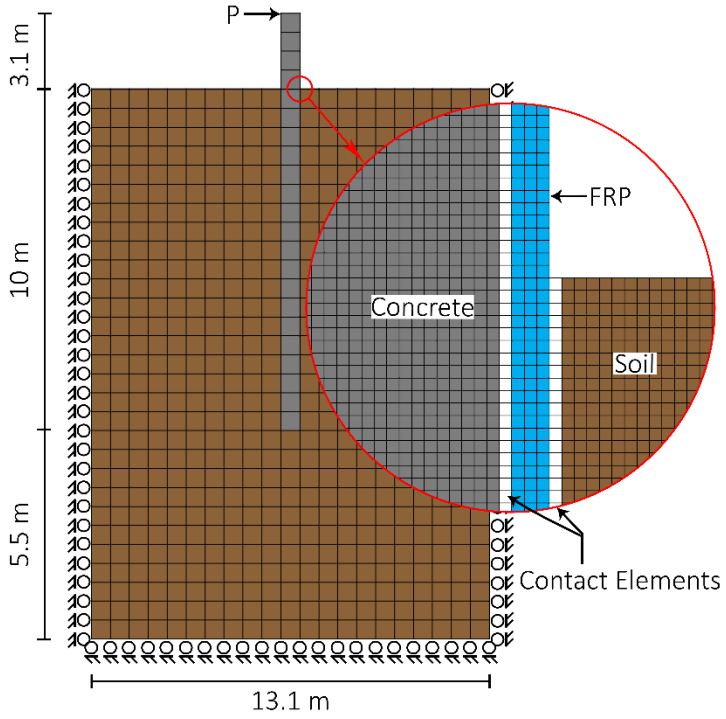

Figure 4.1 Schematic representation of generated mesh for the interface of concrete, FRP laminate and soil in the proposed model (The figure is not scaled).

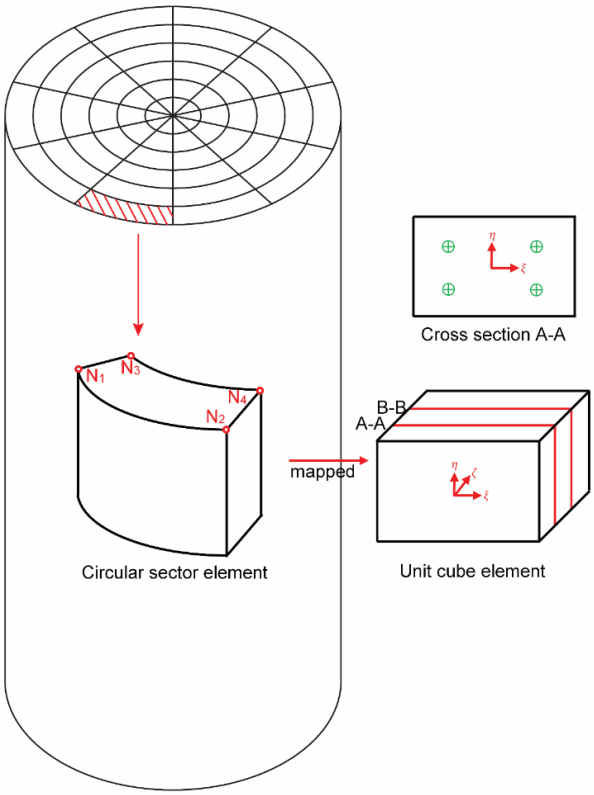

Figure 4.2 Schematic configuration of generated mesh in a horizontal direction and mapping procedure used for quadratic interpolation and extrapolation of NFEA in three dimensions by considering eight Gaussian points

To address the contact problem resulting from the interface of the composite pile and soil, a separate meshes were generated for concrete, soil and contact elements (see Figure 4.1). As can be seen in the figure, the interface of the composite pile and soil is represented by the white areas between the soil and the concrete. The interface was modeled by using the node-to-node contact elements and full bonding between the concrete and FRP laminate was assumed since the shear stress was in the range of 35 to 50 kPa, and bond strength ranged from 510 to 820 kPa, based on research conducted by Helmi et al. (2005). Moreover, the friction and normal stress of the FRP and concrete with soil were considered in the model. It should be noted that the mesh generated was scaled for a schematic illustration of the mesh.

The stress, strain, and displacement matrix values were initialized prior to performing the calculations. The failure of each Gaussian point was checked by applying the first increment of loading. If the Gaussian point has failed, the elastic prediction must be corrected with the elastoplastic stiffness matrix.

4.2.2 LOCAL BUCKLING UNDER AXIAL COMPRESSION

The critical stress for local buckling can be controlled by using the following procedure: An approximate closed form solution for axial loading can be developed to check the local buckling of the pile. According to Batdorf (1947), the following equations can be obtained for a cylinder with a radius of r, wall thickness of t, and length of L, in considering equilibrium in the axial (z), circumferential (θ), and radial (r) directions:

$$\begin{cases} r\dfrac{\partial N_z}{\partial z}+\dfrac{\partial N_{\theta z}}{\partial \theta}=0 \\ r\dfrac{\partial N_{z\theta}}{\partial z}+\dfrac{\partial N_{\theta}}{\partial \theta}=0 \\ \nabla^4 w=\dfrac{1}{D}(p+N_z\dfrac{\partial^2 w}{\partial z^2}+\dfrac{2}{r}N_{z\theta}\dfrac{\partial^2 w}{\partial z\partial\theta}+\dfrac{1}{r^2}N_{\theta}\dfrac{\partial^2 w}{\partial \theta^2}-\dfrac{1}{r}N_{\theta}) \end{cases} \tag{4.1}$$

where w, N, and p represent displacement in the radial direction, applied load per unit length, and lateral pressure, respectively. The plate flexural stiffness per unit length (D) can be defined as:

$$D=\frac{Et^3}{12(1-\nu^2)} \tag{4.2}$$

where E and ν represent the elastic modulus and Poisson's ratio, respectively. For a pure axial load of P, N components can be expressed as:

$$N_z=\frac{P}{2\pi r},\ N_{z\theta}=N_{\theta}=0 \tag{4.3}$$

Introducing these values into Eq. 10 (c) and considering the kinematic and constitutive relationships yields:

$$D\nabla^8 w + \frac{Et}{r^2}\frac{\partial^4 w}{\partial z^4} + \frac{P}{2\pi r}\nabla^4\left(\frac{\partial^2 w}{\partial z^2}\right) = 0 \tag{4.4}$$

The form of solution for this differential equation is:

$$w = \delta\left(\sin\frac{m\pi z}{L}\right)\sin n\theta \tag{4.5}$$

where m represents the number of half waves in the z direction, and n represents the number of entire waves in the θ direction. Thus, the minimum critical stress would be:

$$\sigma_{z,cr} = \frac{\pi^2}{12(1-\nu^2)}\left(\frac{t}{L}\right)^2\left[\frac{(m^2+\bar{n}^2)^2}{m^2} + \frac{12Z^2}{\pi^4}\frac{m^2}{(m^2+\bar{n}^2)^2}\right] \tag{4.6}$$

where $\bar{n} = \frac{nl}{\pi r}$ and Z is a Batdorf parameter which can be expressed as (Batdorf, 1947):

$$Z = \frac{L^2}{rt}\sqrt{1-\nu^2} \tag{4.7}$$

For medium-length cylinders, the smallest critical stress can be estimated by minimizing Eq. 15 with respect to the m and n parameters, as follows:

$$\sigma_{z,cr} = \frac{\pi^2}{12(1-\nu^2)}\left(\frac{t}{L}\right)^2 . \frac{4\sqrt{3}}{\pi^2} Z = 0.577\frac{Et}{r\sqrt{1-\nu^2}} \tag{4.8}$$

4.2.3 Local Buckling under Lateral Soil Pressure

Under an external pressure of p, the applied load components can be expressed as:

$$N_\theta = -pr,\ N_z = N_{z\theta} = 0 \tag{4.9}$$

Introducing these values into Eq. 10 (c) results in:

$$D\nabla^8 w + \frac{Et}{r^2}\frac{\partial^4 w}{\partial z^4} + \frac{p}{r}\nabla^4\left(\frac{\partial^2 w}{\partial\theta^2}\right) = 0 \tag{4.10}$$

The displacement function has the same form as Eq. 14. Similarly, the critical stress would be:

$$\sigma_{\theta,cr} = -\frac{pr}{t} = \frac{\pi^2 E}{12(1-\nu^2)}\left(\frac{t}{L}\right)^2\left[\frac{\left(m+\bar{n}^2\right)^2}{\bar{n}^2} + \frac{12Z^2}{\pi^4\bar{n}^2\left(m+\bar{n}^2\right)^2}\right] \tag{4.11}$$

As can be seen in the equation, one axial wave (m=1) provides the lowest buckling load. Minimizing the term in brackets by trial yields:

$$\sigma_{\theta,cr} = \frac{E}{4(1-\nu^2)}\left(\frac{t}{r}\right)^2 \tag{4.12}$$

The combined pile loading does not result in local buckling if the following formula is satisfied (Odland, 1978):

$$C_{z\theta} = \left(\frac{\sigma_z}{\sigma_{z,cr}}\right)^2 + \left(\frac{\sigma_\theta}{\sigma_{\theta,cr}}\right)^2 \le 1 \tag{4.13}$$

If the local buckling factor ($C_{z\theta}$) is less than one, it can be concluded that applying both lateral soil pressure and axial loading to a hollow pile will result in a greater probability of buckling than is the case with pure axial compression. Thus, if a hollow pile fails due to buckling at the ground surface, there is a higher chance of buckling at the depth of maximum axial stress.

4.2.4 MATERIAL PROPERTIES

Table 4.1 presents the mechanical properties of soil, concrete, and FRP used in the proposed model: the elastic modulus (E), Poisson's ratio (ν), cohesion (c), and the angle of internal friction (ϕ). In the model, the friction coefficient (μ) between FRP tube and soil was assumed to be 0.3 while the value of 5 was considered for the interface of concrete and FRP tube to account for full bonding of this interface (Alexandria, 1986). The initial modulus of elasticity (E) for concrete is based on the following equation related to the requirements of Committee 318 of the American Concrete Institute (ACI) (2014):

$$E_c = 4700\sqrt{f'_c} \tag{4.14}$$

Table 4.1 Mechanical parameters used in the proposed model

	Parameter	Concrete	Soil		FRP
			Sand	Clay	
Elasticity	E (MPa)	30,241	9.32	8.15	15,162
	ν	0.2	0.29	0.3	0.32
Plasticity	c (MPa)	6.43	0.1	5.0	-
	ϕ (deg)	55.51	34.0	29.0	-

where E_c and f'_c represent the elastic modulus and the compressive strength of concrete in MPa, respectively. The parameters of the Mohr-Coulomb failure criterion were obtained by using the following equations (Zhao, 2000):

$$\begin{cases} \varphi = \sin^{-1}\left(\dfrac{f'_c - f'_t}{f'_c + f'_t}\right) \\ c = \dfrac{\sqrt{f'_c f'_t}}{2} \end{cases} \tag{4.15}$$

where f'_c and f'_t represent the uniaxial compressive and tensile strength of concrete, which can be expressed as (ACI committee 318, 2014):

$$f'_t = 0.62\sqrt{f'_c} \tag{4.16}$$

4.3 Model Calibration

To calibrate the parameters of the proposed model, experimental field test results were obtained from Fam et al. (2003). The composite piles were concrete-filled glass fiber-reinforced polymer (GFRP) tubes considered for a highway bridge on route 40 in Virginia, with an outer diameter and tube thickness of 62.48 cm (24.6 in.) and 5.41 mm (0.213 in.), respectively. The profile of the surrounding soil at the site was composed of various soil layers, including sand and clay. The soil conditions were loose at the top and stiff at the bottom of the soil layers. In Figure 4.3, the cross-section of the concrete pile is presented along the soil profile, as well as an arbitrary cross section, A-A. The total length of the composite pile was 13.1 m, including the length of the pile that was not covered by soil. The compressive strength of the concrete used was reported to be 41.4 MPa by Fam et al. (2003).

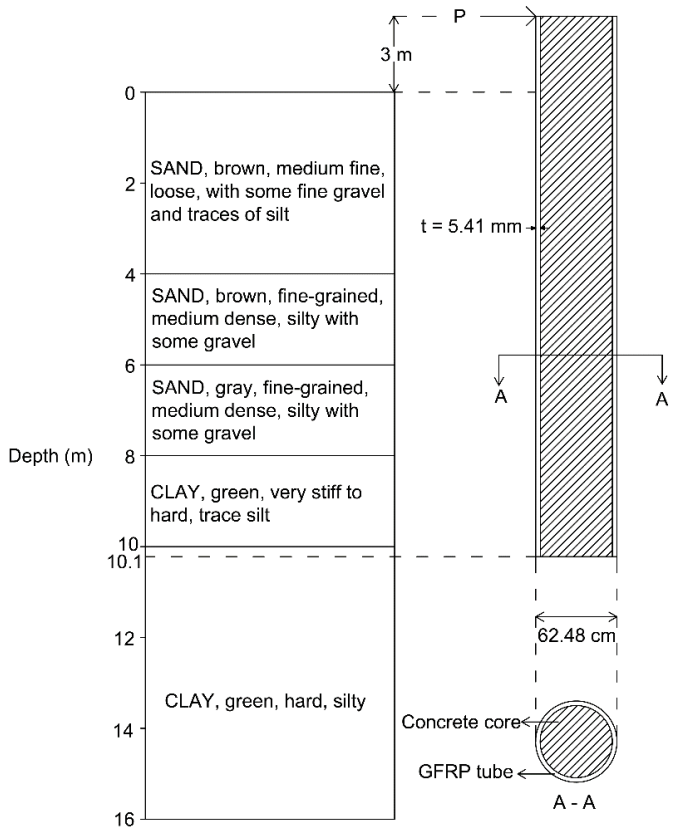

Figure 4.3 Soil and composite pile profiles along the depth based on Fame et al. (2003)

Model calibration graphs are presented in Figure 4.4, showing the lateral deflection for different lateral loads applied at the top of the composite pile: 48.9, 80.1, 93.5, and 120.1 kN. As shown in the figure, the lateral deflection of the composite pile below a depth of seven meters is approximately zero. Based on the experimental and numerical curves, it can be seen that the modeling results are in good agreement with the experimental data. As a result, the model can be used to perform parametric studies, as described below.

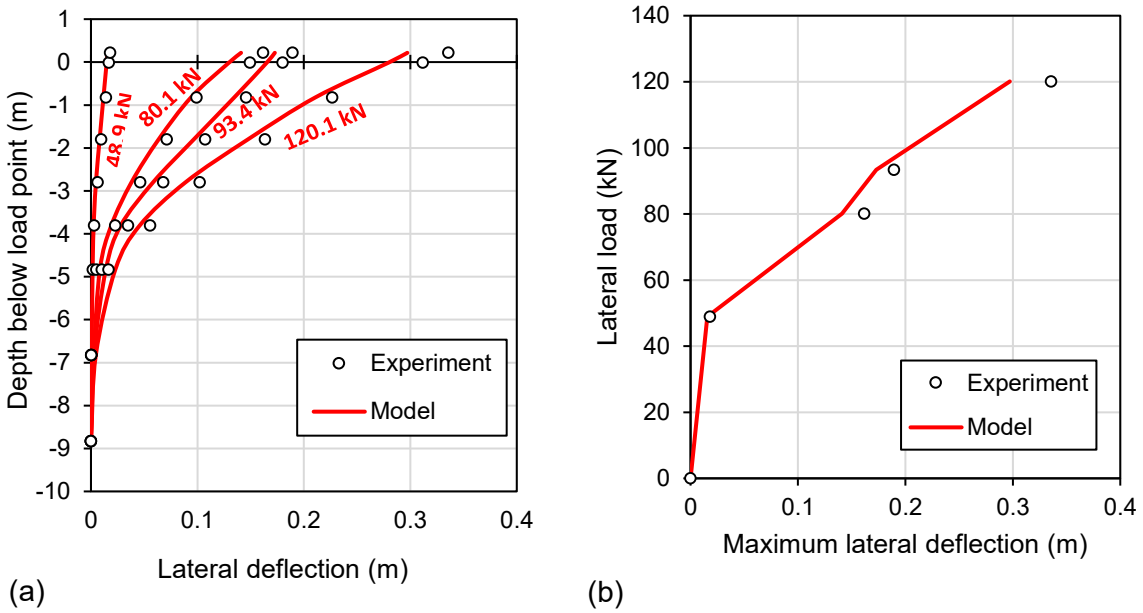

Figure 4.4 Model verification against field data of lateral deflection along the length of CFFT pile tested by Fam et al. (2003) at different lateral load levels ranging from 48.9 to 120.1 kN

4.4 Sensitivity Analysis for Model Calibration

To investigate the effect of the coefficient of friction on the calibration of the proposed model, a sensitivity analysis was conducted by using different coefficients of friction including 0.1, 0.3 and 0.5. The corresponding results of sensitivity analysis for maximum lateral deflection at the depth of 1.44 cm from soil surface are shown in Figure 4.5. As can be seen in the figure, the assumption of $\mu = 0.3$ will not affect the calibration results significantly.

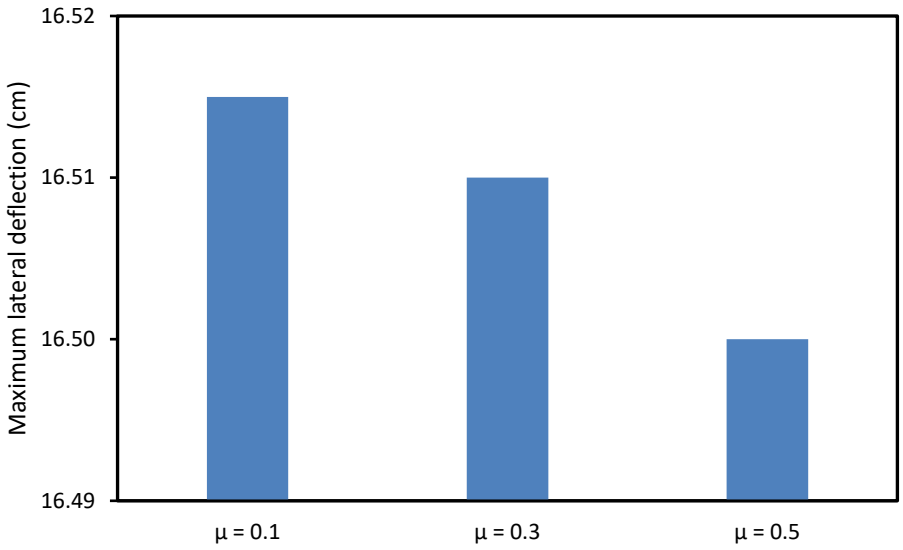

Figure 4.5 Maximum lateral deflection for different coefficients of friction including 0.1, 0.3 and 0.5 at the depth of 1.44 cm from soil surface

4.5 Parametric Study

The effect of different model parameters including height-to-diameter ratio of specimens, FRP tube thickness, concrete strength and surrounding soil was investigated on the moment, shear, axial curves as well as lateral deflection and FRP and soil stresses of composite piles along the depth under a 100 kN of applied load.

4.5.1 Effect of length/diameter ratio

As shown in Figure 4.6, three different length/diameter (L/D) ratios: 15, 20, and 25, were used in the proposed model to investigate the effect of geometry on the lateral deformation of composite piles under a constant lateral load of 100 kN. A constant composite pile length (L) of 13.1 m was assumed, while the diameter (D) was changed in order to compare the results. As can be seen in the figure, the greater the L/D ratio at a certain depth, the greater the lateral deflection of the composite pile.

The proposed model was used to examine the effect of the length/diameter (L/D) ratio of CFFT piles on the bending moment, shear force, axial load, and axial tensile stress of the FRP tube, and on the lateral deformation plotted against the normalized depth (Z/D). The results of the corresponding parametric study are shown in Figure 4.6. It can be seen that an increase in D (i.e., a decrease in L/D) results in an increased maximum moment, shear force and axial load for the CFFT pile. Moreover, the normalized depth at which the maximum moment occurs decreases with lower L/D values. The bending capacity of CFFT piles with a diameter of 0.62 m is reported to be approximately 502 kN.m (Fam & Rizkalla, 2001a). Higher shear force and axial load values were obtained for composite piles with lower L/D ratios, as shown in Figure 4.6 (e) and (f). In addition, Figure 4.6 (b) shows an increase in the FRP axial tensile stress at the extreme tension fiber with a higher L/D ratio, although the trend was not consistent. In Figure 4.6 (a), the effect of L/D values on the lateral deflection is depicted. Figure 4.6 (c) shows that an increasing L/D ratio also results in greater stresses in the soil.

4.5.2 Effect of FRP tube thickness

To determine the effect of FRP thickness (t) on the mechanical behavior of CFFT piles, different FRP thicknesses, including 5, 7, and 9 mm, were studied. In addition to providing better passive confining pressure for the CFFT piles, a thicker FRP layer also reduces the lateral pile deformation due to the greater strength of the composite material. The maximum lateral CFFT pile deflections obtained at ground level were 28.4 and 27.8 cm, for FRP thicknesses of 9 and 5 mm, respectively. Increasing the thickness of the FRP laminate also resulted in a small increase (1-3%) in the maximum FRP tensile stress, and in the maximum soil compressive stress. Moreover, a five percent increase in the maximum CFFT pile moment was obtained by increasing the FRP thickness from 5 to 9 mm. The maximum shear along the length of the composite pile was not noticeably affected by the change in thickness. Therefore, the effect of FRP thickness was not

found to be significant with regard to CFFT pile mechanical properties.

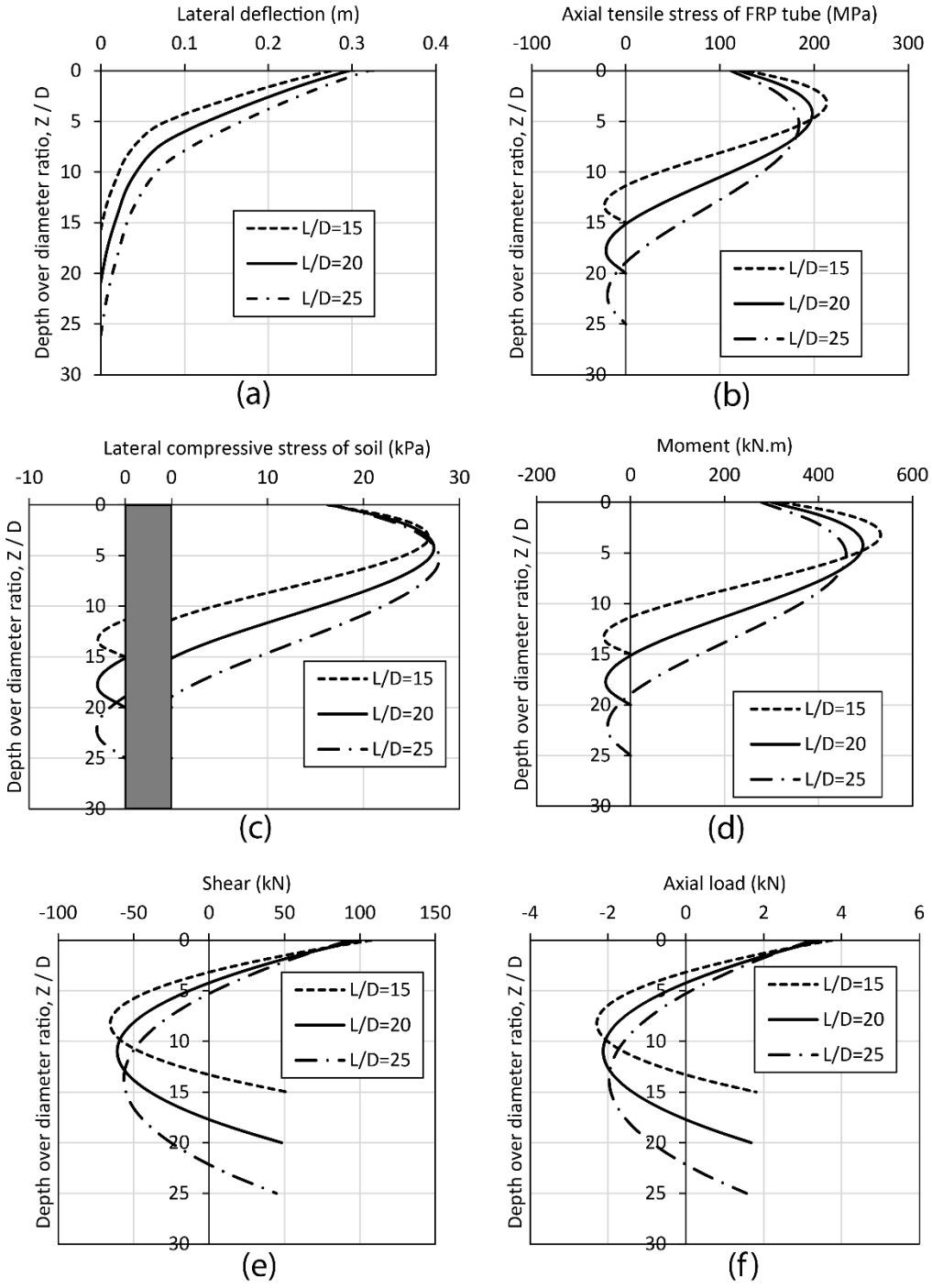

Figure 4.6 Effect of length/diameter (L/D) ratio on the behavior of CFFT pile under lateral load 100 kN: (a) lateral deformation; (b) axial tensile stress of FRP at the extreme tension fiber; (c) soil compressive stress; (d) bending moment; (e) shear force;

and (f) axial force

4.5.3 EFFECT OF CONCRETE STRENGTH

To evaluate the effect of concrete strength on the maximum lateral deflection, maximum moment, maximum lateral soil compressive stress, and maximum axial FRP stress, six different concrete strength values, ranging from 0 to 55 MPa, were used with lateral loads of 12, 50 and 100 kN. The corresponding graphs are presented in Figure 4.7. With a lateral load of 100 kN, for concrete strengths of 30, 40 and 50 MPa, the maximum CFFT pile lateral deflections at the soil surface were found to be 32.7, 29.5 and 27.3 cm, respectively. Increasing the concrete strength from 25 to 55 MPa decreased the maximum axial FRP stress and the maximum moment by 14% to 15% and resulted in a five percent reduction in the maximum lateral compressive soil stress.

The small degree of influence may be due to the fact that elastic properties were mainly affected, and the plastic properties of concrete were not the primary factor in controlling the results. It should be mentioned that in most cases concrete strengths less than 25 MPa were not used, because these resulted in rupturing of the FRP tube. Hence, the effects of concrete strengths less than 25 MPa were investigated only under a small lateral load of 12 kN and 50 kN, as illustrated in Figure 4.7. For a lateral load of 100 kN, with greater concrete strengths, the maximum lateral CFFT pile deflection was reduced by approximately 18%, while the maximum FRP and soil stress decreased by approximately 20%. In Figure 4.7 (b), in the 100 kN curve the maximum moment exhibits a reduction of almost ten percent.

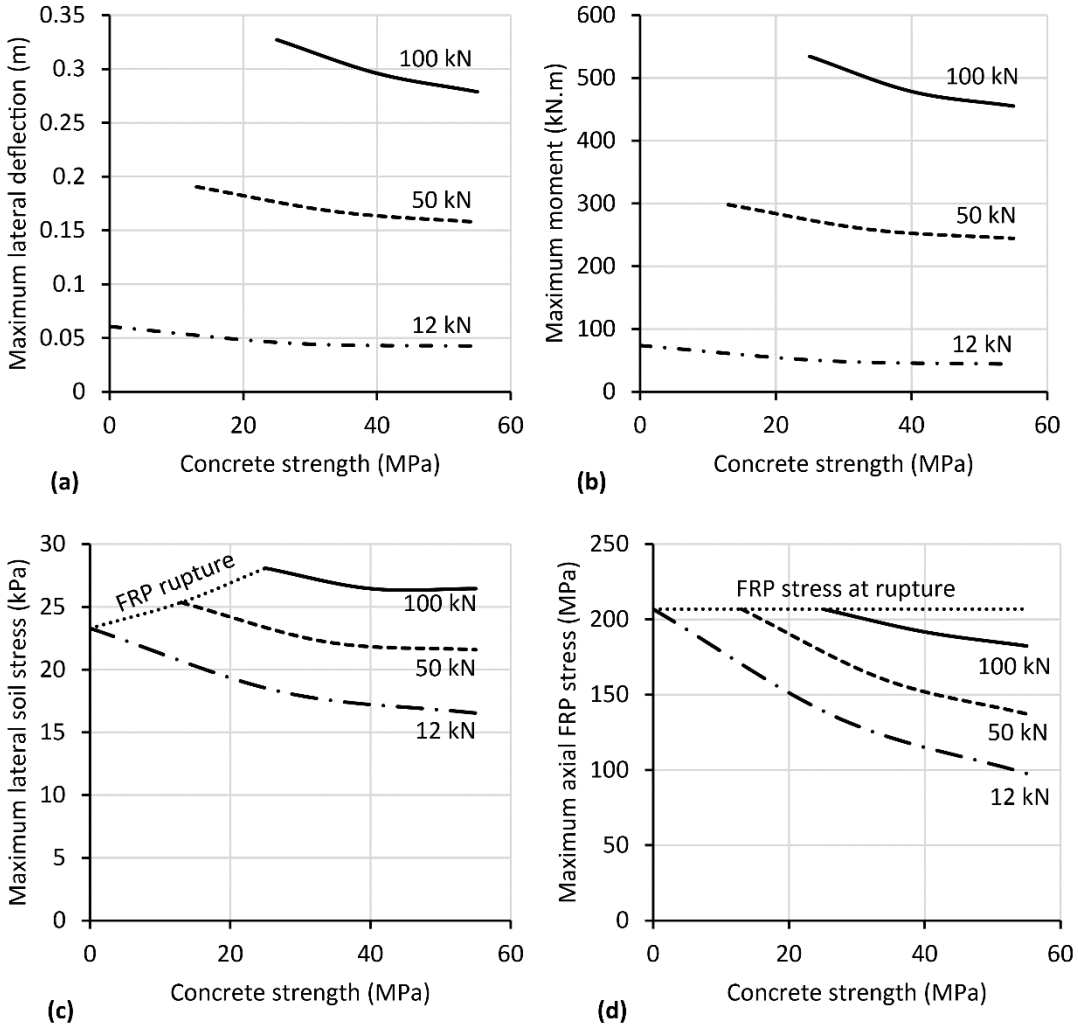

Figure 4.7 Effect of concrete strength on: (a) maximum lateral deflection; (b) moment; (c) lateral soil stress; and (d) axial FRP stress of CFFT pile under lateral loads of 12, 50 and 100 kN

4.5.4 EFFECT OF SURROUNDING SOIL

The effect of soil type was investigated by using the numerical results for three different soil types, as shown in Figure 4.8. The elastic moduli of the loose, medium, and dense sand used in this parametric study were 10, 30, and 60 MPa, respectively. The friction angle (φ) values related to the Mohr-Coulomb failure criterion were 32°, 36°, and 40° for loose, medium, and dense sand, respectively. As shown in Figure 4.8 (a), the maximum lateral deflections of loose, medium, and

dense sand were 26.9, 29.5, and 32 cm, respectively. As can be seen in Figure 4.8 (b), denser surrounding soil decreased the maximum FRP axial stress by 17.4%. Similarly, the maximum moment was reduced by approximately 17%, as shown in Figure 4.8 (d). Figure 4.8 (c) shows that the maximum soil stress decreased by approximately 7%. Furthermore, the shear and axial load were reduced by nearly 6% to 8%, as seen in Figure 4.8 (e) and (f). Thus, it can be concluded the effect of pile diameter and concrete strength is more noticeable than that of other parameters such as soil type and FRP thickness. Cohesionless soil such as sand collapses and flows with the composite pile upon reaching an active state, as the pile is laterally loaded. Thus, the gap in the interface is negligible in comparison to the pile displacement. Likewise, the change in soil stress during pile driving is negligible in comparison to changes in soil stress due to lateral loading of the composite pile (Achmus et al., 2009). For this reason, the effect of pile installation is ignored in the model.

4.5.5 Effect of Applied Load's Position from Soil Surface

To obtain the normalized value of applied load's position from soil surface (e), the ratio of the pile height above the ground (h) to the embedded length of the pile in the soil (L_S) was considered. The effect of this parameter on the maximum lateral deflection, maximum moment, maximum lateral soil stress, and maximum axial FRP stress was investigated. The results are presented in Figure 4.9. It can be seen that increasing e from 0 to 0.3 results in a much greater increase in maximum lateral deflection and maximum moment for a lateral load of 100 kN, than for a lateral load of 12 kN. However, a lower rate of increase is seen in the maximum lateral soil stress and maximum axial FRP stress, due to the fact that the greater the height of the pile above ground level, the more FRP local buckling occurs in the pile. As illustrated in Figure 4.9, an increase in lateral load has a significant impact on the results with respect to the higher values of e.

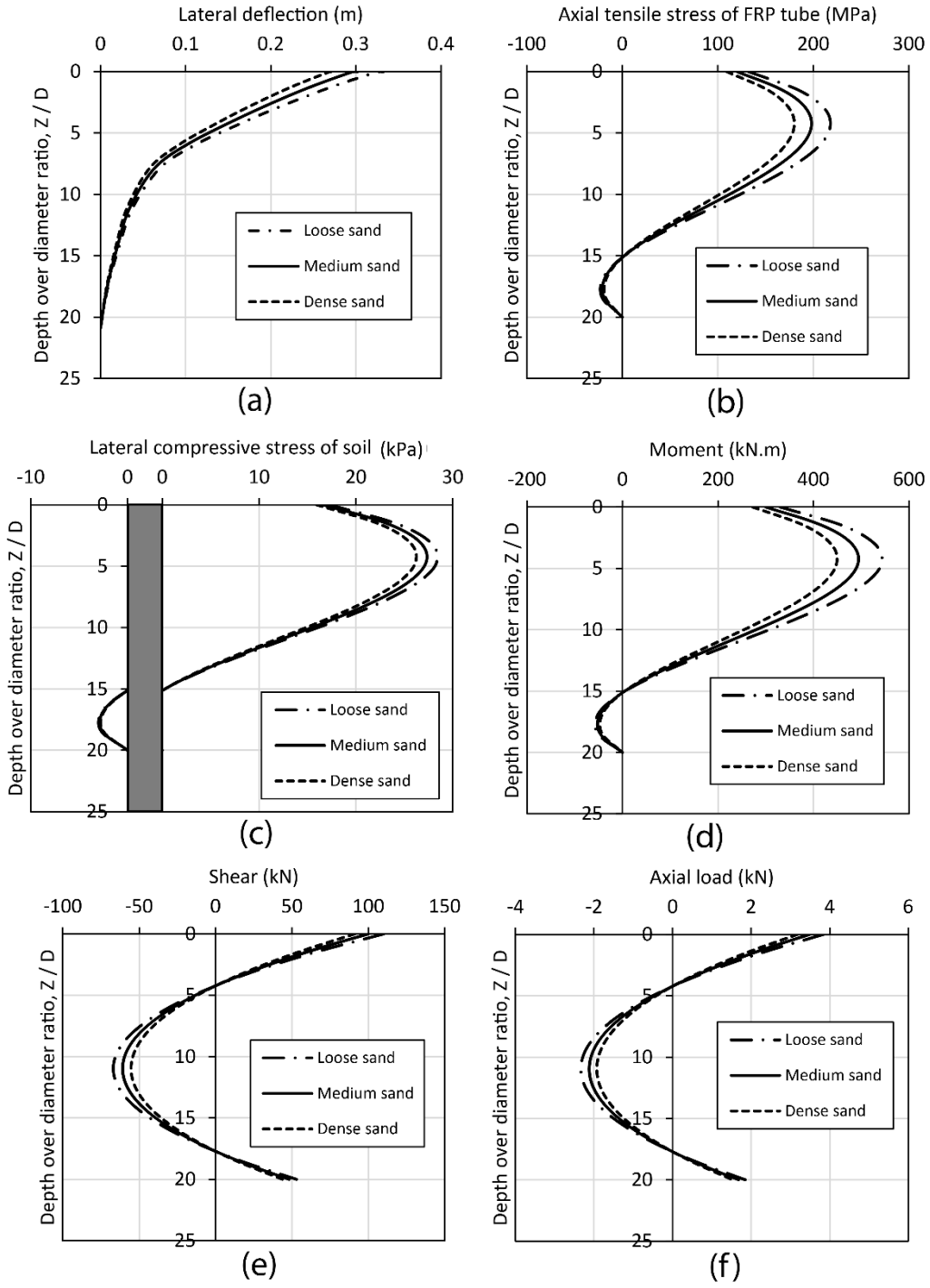

Figure 4.8 Effect of soil type on the behavior of CFFT pile under lateral load 100 kN: (a) lateral deformation; (b) axial tensile stress of FRP at the extreme tension fiber; (c) soil compressive stress; (d) bending moment; (e) shear force; and (f) axial force

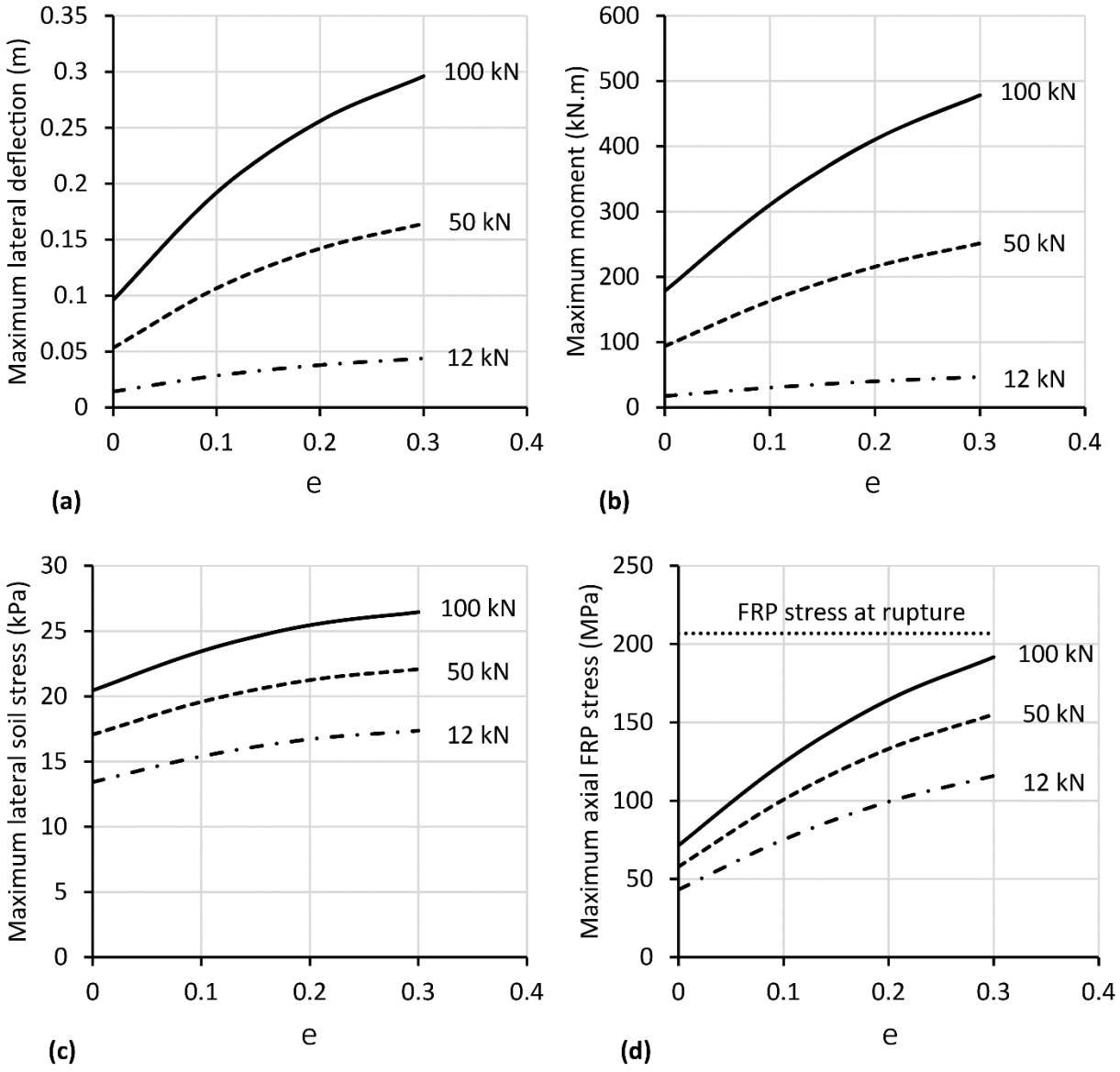

Figure 4.9 Effect of normalized applied load's position from soil surface (e) on: (a) maximum lateral deflection; (b) moment; (c) lateral soil stress; and (d) axial FRP stress of CFFT pile under lateral loads of 12, 50 and 100 kN

4.5.6 LOCAL BUCKLING OF HOLLOW FRP PILE

Introducing the FRP tube values obtained by Fam et al. (2003) into Eq. 17 yields $\sigma_{z,cr}$=161.4 MPa, which is greater than σ_z=120.2 MPa at the ground surface. In this case, local buckling at ground level is not the controlling factor for hollow FRP tube or CFFT pile failure. However, introducing the pile values into Eq. 21 yields $\sigma_{\theta,cr}$=1.29 MPa, whereas based on the values shown in the graphs σ_θ=27.81 kPa. In this case, local buckling will control failure under combined loading at the level of maximum FRP stress. This can be estimated by using the following formula:

$$C_{z\theta} = \left(\frac{\sigma_z}{\sigma_{z,cr}}\right)^2 + \left(\frac{\sigma_\theta}{\sigma_{\theta,cr}}\right)^2 = 1.49 > 1 \tag{4.17}$$

Table 4.2 shows local buckling factor ($C_{z\theta}$) values corresponding to different L/D ratios and FRP thicknesses (t). It can be seen that a pile with L/D=15 is very susceptible to local buckling, whereas FRP tubes with L/D=25 or a wall thickness of 9 mm are not subject to buckling. It should be noted that these values are overestimated for pure bending, since not all of the cross-section is under maximum compression.

Table 4.2 Local buckling factor ($C_{z\theta}$) values corresponding to different L/D ratios and FRP thicknesses (t)

Depth	L/D			t (mm)		
	15	20	25	5	7	9
Ground level	1.5	0.7	0.4	0.7	0.4	0.2
Maximum FRP stress	4.0	1.9	1.1	1.9	1.0	0.7

CHAPTER 5 CONCLUSIONS AND RECOMMENDATIONS

5.1 CONCLUSIONS

In this research, a novel numerical model was developed to predict the behavior of concrete-filled FRP tube (CFFT) piles interacting with a soil foundation under lateral loading conditions. The model, based on nonlinear finite element analysis (NFEA) and the disturbed state concept (DSC), is a damage model that considers material and geometrical nonlinearity in addition to the interface of soil and FRP. A case study of a highway bridge on route 40 in Virginia was used to verify the model. Furthermore, a comprehensive parametric study was conducted to investigate the effect on CFFT pile behavior of the pile length to diameter ratio, FRP thickness, concrete strength, and soil strength. Different concrete strengths, including 32, 41, and 55 MPa, were considered with 100 kN lateral loading. To examine the behavior of a hollow tube (having zero concrete strength) without failure, a 10 kN horizontal load was applied to the pile. The following conclusions can be drawn from this research:

- The slenderness of CFFT piles has a significant effect on their mechanical behavior. For example, decreasing the L/D ratio from 25 to 15 resulted in an 18% increase in the maximum moment.

- FRP thickness was found to be the least significant parameter in the parametric study. For instance, increasing the thickness from 5 to 9 mm resulted in only a five percent increase in the maximum moment of a CFFT pile.

- With a lateral load of 100 kN, decreasing the concrete strength from 55 to 25 MPa resulted in a 15% increase in the maximum moment of a CFFT pile. Furthermore, with an applied load of 10 kN, a 10% increase in the maximum moment was obtained by removing the

concrete core with compressive strength of 20 MPa.

- In a parametric study of surrounding soil, dense sand with a friction angle of 40° resulted in a maximum moment 17% greater than that found for loose sand with a friction angle of 32°.

- Local buckling is a major design factor for FRP tubes at the maximum FRP stress level rather than at the ground surface. For instance, the FRP tubes with L/D=15 is very susceptible to local buckling, while FRP tubes with L/D=25 or a wall thickness of 9 mm are not subject to buckling. To address this issue, a low-strength internal material could be used to prevent local buckling of the pile.

- The DSC damage model was able to model the softening behavior of concrete and soil by considering the RI and FA responses.

5.2 RECOMMENDATIONS

The following suggestions are recommended for further investigations in order to gain a better understanding of CFFTs:

- The local buckling of concrete piles can be studied with and without FRP tube followed by an experimental test to develop a formulation for local buckling since the equations provided in this research were provided for isotropic material such as steel tube.

- CFFTs can be modeled using different plasticity models such as Drucker Prager to compare the accuracy and applicability of different plasticity models.

- The FRP tube layers can be studied with orthotropic assumption supported by experimental tests in which FRP tube governs the results.

- The effect of axial load along with lateral load on the capacity of composite pile can be studied.

- Adding a low-strength internal material such as concrete with aggregates partially replaced by tire-derived aggregates (TDA) may prevent local pile buckling, providing a cost-effective and environment-friendly solution. Further research is needed to investigate the local buckling of FRP piles filled with other low-strength materials in addition to concrete.

BIBLOGRAPHY

Abu-Farsakh, M., Souri, A., Voyiadjis, G., & Rosti, F. (2017). Comparison of static lateral behavior of three pile group configurations using three-dimensional finite element modeling. *Canadian Geotechnical Journal*, *55*(1), 107–118. https://doi.org/10.1139/cgj-2017-0077

Abu-Farsakh, M., Yu, X., Pathak, B., Alshibli, K., & Zhang, Z. (2011). Field Testing and Analyses of a Batter Pile Group Foundation under Lateral Loading. *Transportation Research Record*, *2212*(1), 42–55. https://doi.org/10.3141/2212-05

Achmus, M., Kuo, Y.-S., & Abdel-Rahman, K. (2009). Behavior of monopile foundations under cyclic lateral load. *Computers and Geotechnics*, *36*(5), 725–735.

ACI committee 318. (2014). Building Code Requirements for Structural Concrete and Commentary. *American Concrete Institute, Farmington Hills, MI*, 520.

Akhaveissy, A. H., Desai, C. S., Sadrnejad, S. A., & Shakib, H. (2009). Implementation and comparison of generalized plasticity and disturbed state concept for load-deformation behavior of foundation. *Scientia Iranica Transaction A: Civil Engineering*, *16*(3), 189–198. Retrieved from http://www.scientiairanica.com/PDF/Articles/00001027/Akhaveisi.pdf

Alexandria, V. (1986). Foundations & Earth Structures. *Naval Facilities Engineering Command*.

Allotey, N., & El Naggar, M. H. (2008). A numerical study into lateral cyclic nonlinear soil–pile response. *Canadian Geotechnical Journal*, *45*(9), 1268–1281.

Ashour, M., Pilling, P., & Norris, G. (2004). Lateral behavior of pile groups in layered soils. *Journal of Geotechnical and Geoenvironmental Engineering*, *130*(6), 580–592.

Basack, S., & Nimbalkar, S. (2018). Measured and Predicted Response of Pile Groups in Soft Clay Subjected to Cyclic Lateral Loading. *International Journal of Geomechanics*, *18*(7),

04018073. https://doi.org/10.1061/(ASCE)GM.1943-5622.0001188

Batdorf, S. B. (1947). A simplified method of elastic-stability analysis for thin cylindrical shells. *National Advisory Committee for Aeronautics*.

Bhowmik, D., Baidya, D. K., & Dasgupta, S. P. (2016). A numerical and experimental study of hollow steel pile in layered soil subjected to vertical dynamic loading. *Soil Dynamics and Earthquake Engineering*, *85*, 161–165. https://doi.org/10.1016/j.soildyn.2016.03.017

Bohn, C., Dos-Santos, A. L., & Frank, R. (2015). Development of Axial Pile Load Transfer Curves Based on Instrumented Load Tests. *Geotechnical and Geological Engineering*, *143*(1), 1–15. https://doi.org/10.1061/(ASCE)GT.1943-5606.0001579.

Brinkgreve, R. B. J., Swolfs, W. M., & Engine, E. (2007). Plaxis 3D foundation version 2 user's manual. *Plaxis BV, Netherlands*.

Brown, D. A., & Shie, C.-F. (1990). Three dimensional finite element model of laterally loaded piles. *Computers and Geotechnics*, *10*(1), 59–79.

Chae, K. S., Ugai, K., & Wakai, A. (2004). Lateral resistance of short single piles and pile groups located near slopes. *International Journal of Geomechanics*, *4*(2), 93–103.

Comodromos, E. M., & Pitilakis, K. D. (2005). Response evaluation for horizontally loaded fixed-head pile groups using 3-D non-linear analysis. *International Journal for Numerical and Analytical Methods in Geomechanics*, *29*(6), 597–625.

Desai, C. S. (2001). *Mechanics of Materials and Interfaces: The Disturbed State Concept*. CRC Press.

Desai, C. S. (2015). Constitutive modeling of materials and contacts using the disturbed state concept: Part 1 – Background and analysis. *Computers & Structures*, *146*, 214–233. https://doi.org/10.1016/j.compstruc.2014.07.018

Dias, T. G. S., & Bezuijen, A. (2018). Load-Transfer Method for Piles under Axial Loading and Unloading. *Journal of Geotechnical and Geoenvironmental Engineering*, *144*(1), 04017096. https://doi.org/10.1061/(ASCE)GT.1943-5606.0001808

Dijkstra, J., Broere, W., & Heeres, O. M. (2011). Numerical simulation of pile installation. *Computers and Geotechnics*, *38*(5), 612–622.

El-Nemr, A. M., Ashour, O., & Hekal, G. M. (2016). *Dynamic response of confined concrete piles with FRP tubes in sandy soil using finite element modeling*.

Fam, A., Flisak, B., & Rizkalla, S. (2003). Experimental and analytical modeling of concrete-filled FRP tubes subjected to combined bending and axial loads. *ACI Struct. J*, *100*(4), 499–509.

Fam, A., Pando, M., Filz, G., & Rizkalla, S. (2003). Precast piles for Route 40 bridge in Virginia using concrete filled FRP tubes. *PCI Journal*, *48*(3), 32–45.

Fam, A., & Rizkalla, S. (2001a). Behavior of axially loaded concrete-filled circular FRP tubes. *ACI Structural Journal*, *98*(3), 280–289.

Fam, A., & Rizkalla, S. (2001b). Confinement Model for Axially Loaded Concrete Confined by Circular Fiber-Reinforced Polymer Tubes. *ACI Structural Journal*, *98*(4). https://doi.org/10.14359/10288

Fam, A., Schnerch, D., & Rizkalla, S. (2005). Rectangular filament-wound glass fiber reinforced polymer tubes filled with concrete under flexural and axial loading: experimental investigation. *Journal of Composites for Construction*, *9*(1), 25–33.

Gazioglu, S. M., & O'Neill, M. W. (1984). Evaluation of py relationships in cohesive soils. *Analysis and Design of Pile Foundations*, 192–213. ASCE.

Han, F., Prezzi, M., & Salgado, R. (2017). Energy-Based Solutions for Nondisplacement Piles

Subjected to Lateral Loads. *International Journal of Geomechanics*, *17*(11), 04017104. https://doi.org/10.1061/(ASCE)GM.1943-5622.0001012

Hazzar, L., Hussien, M. N., & Karray, M. (2017). Vertical load effects on the lateral response of piles in layered media. *International Journal of Geomechanics*, *22*(9), 1–11. https://doi.org/10.1061/(ASCE)GM.1943-5622.0000970

Heidari, M., Jahanandish, M., El Naggar, H., & Ghahramani, A. (2014). Nonlinear cyclic behavior of laterally loaded pile in cohesive soil. *Canadian Geotechnical Journal*, *51*(2), 129–143. https://doi.org/10.1139/cgj-2013-0099

Helmi, K., Fam, A., & Mufti, A. (2005). Field installation, splicing, and flexural testing of hybrid FRP/concrete piles. *Special Publication*, *230*, 1103–1120.

Isenhower, W. M., Vasquez, L. G., & Wang, S.-T. (2014). Analysis of settlement-induced bending moments in battered piles. In *From Soil Behavior Fundamentals to Innovations in Geotechnical Engineering: Honoring Roy E. Olson* (pp. 497–511).

Iskander, M., Mohamed, A., & Hassan, M. (2002). Durability of recycled fiber-reinforced polymer piling in aggressive environments. *Transportation Research Record*, *1808*(1), 153–161.

Khoei, A. (2005). Computational Plasticity in Powder Forming Processes. In *Computational Plasticity in Powder Forming Processes*. https://doi.org/10.1016/B978-008044636-3/50008-0

Khoei, A. (2010). *Computational Plasticity in Powder Forming Processes*. Retrieved from https://books.google.com/books?id=TKEQjVGTSHcC&pgis=1

Kim, Y., & Jeong, S. (2011). Analysis of soil resistance on laterally loaded piles based on 3D soil–pile interaction. *Computers and Geotechnics*, *38*(2), 248–257.

Ladhane, K. B., & Sawant, V. A. (2016). Effect of Pile Group Configurations on Nonlinear Dynamic Response. *International Journal of Geomechanics*, *16*(1), 04015013. https://doi.org/10.1061/(ASCE)GM.1943-5622.0000476

Leung, Y. F., Klar, A., & Soga, K. (2010). Theoretical Study on Pile Length Optimization of Pile Groups and Piled Rafts. *Journal of Geotechnical and Geoenvironmental Engineering*, *136*(2), 319–330. https://doi.org/10.1061/(ASCE)GT.1943-5606.0000206

Matlock, H. (1970). Correlations for design of laterally loaded piles in soft clay. *Offshore Technology in Civil Engineering Hall of Fame Papers from the Early Years*, 77–94.

Mirmiran, A., & Shahawy, M. (1996). A new concrete-filled hollow FRP composite column. *Composites Part B: Engineering*, *27*(3–4), 263–268.

Mirmiran, A., & Shahawy, M. (1997). Behavior of concrete columns confined by fiber composites. *Journal of Structural Engineering*, *123*(5), 583–590.

Mirmiran, A., Zagers, K., & Yuan, W. (2000). Nonlinear finite element modeling of concrete confined by fiber composites. *Finite Elements in Analysis and Design*, *35*(1), 79–96.

Mohamed, H. M., & Masmoudi, R. (2010a). Axial load capacity of concrete-filled FRP tube columns: Experimental versus theoretical predictions. *Journal of Composites for Construction*, *14*(2), 231–243.

Mohamed, H. M., & Masmoudi, R. (2010b). Flexural strength and behavior of steel and FRP-reinforced concrete-filled FRP tube beams. *Engineering Structures*, *32*(11), 3789–3800.

Muqtadir, A., & Desai, C. S. (1986). Three-dimensional analysis of a pile-group foundation. *International Journal for Numerical and Analytical Methods in Geomechanics*, *10*(1), 41–58.

Nelson, M., Ching Lai, Y., & Fam, A. (2008). Moment Connection of Concrete-Filled Fiber

Reinforced Polymer Tubes by Direct Embedment into Footings. In *Advances in Structural Engineering - ADV STRUCT ENG* (Vol. 11). https://doi.org/10.1260/136943308786412023

Odland, J. (1978). Buckling resistance of unstiffened and stiffened circular cylindrical shell structures. *Norwegian Maritime Research*, *6*(3).

Ozbakkaloglu, T. (2013). Compressive behavior of concrete-filled FRP tube columns: Assessment of critical column parameters. *Engineering Structures*, *51*(Supplement C), 188–199. https://doi.org/https://doi.org/10.1016/j.engstruct.2013.01.017

Ozbakkaloglu, T., & Oehlers, D. J. (2008). Manufacture and testing of a novel FRP tube confinement system. *Engineering Structures*, *30*(9), 2448–2459. https://doi.org/https://doi.org/10.1016/j.engstruct.2008.01.014

Pando, M. A., Ealy, C. D., Filz, G. M., Lesko, J. J., & Hoppe, E. J. (2006). *A laboratory and field study of composite piles for bridge substructures*.

Poulos, H. G., & Davis, E. H. (1980). *Pile Foundation Analysis and Design, Series in Geotechnical Engineering, Edited by TW Lambe and RV Whitman*. John Wiley and Sons, Inc., New York.

Prasad, Y. V. S. N., & Chari, T. R. (1999). Lateral Capacity of Model Rigid Piles In Cohesionless Soils. *Soils and Foundations*, *39*(2), 21–29. https://doi.org/10.3208/sandf.39.2_21

Reese, L. C., Cox, W. R., & Koop, F. D. (1974). Analysis of laterally loaded piles in sand. *Offshore Technology in Civil Engineering Hall of Fame Papers from the Early Years*, 95–105.

Roddenberry, M., Mtenga, P., & Joshi, K. (2014). *Investigation of Carbon Fiber Composite Cables (CFCC) in Prestressed Concrete Piles*. Retrieved from https://trid.trb.org/view.aspx?id=1308711

Russo, G. (2016). A method to compute the non-linear behaviour of piles under horizontal loading. *Soils and Foundations*, *56*(1), 33–43.

Sadeghian, P., & Fam, A. (2010). Bond-Slip Analytical Formulation toward Optimal Embedment of Concrete-Filled Circular FRP Tubes into Concrete Footings. *Journal of Engineering Mechanics*, *136*(4), 524–533. https://doi.org/10.1061/(ASCE)EM.1943-7889.0000091

Sadeghian, P., & Fam, A. (2011). Closed-Form Model and Parametric Study on Connection of Concrete-Filled FRP Tubes to Concrete Footings by Direct Embedment. *Journal of Engineering Mechanics*, *137*(5), 346–354. https://doi.org/10.1061/(ASCE)EM.1943-7889.0000231

Sadeghian, P., Yu, C. L., & Fam, A. (2011). Testing and Modeling of a New Moment Connection of Concrete-Filled FRP Tubes to Footings under Monotonic and Cyclic Loadings. *Journal of Composites for Construction*, *15*(4), 653–662. https://doi.org/10.1061/(ASCE)CC.1943-5614.0000198

Souri, A., Abu-Farsakh, M., & Voyiadjis, G. (2015). Study of static lateral behavior of battered pile group foundation at I-10 Twin Span Bridge using three-dimensional finite element modeling. *Canadian Geotechnical Journal*, *53*(6), 962–973. https://doi.org/10.1139/cgj-2015-0345

Su, D., & Zhou, Y. G. (2015). Effect of Loading Direction on the Response of Laterally Loaded Pile Groups in Sand. *International Journal of Geomechanics*, *16*(2), 4015051. https://doi.org/10.1061/(ASCE)GM.1943-5622.0000544

Suleiman, M. T., Ni, L., Helm, J. D., & Raich, A. (2014). Soil-pile interaction for a small diameter pile embedded in granular soil subjected to passive loading. *Journal of Geotechnical and Geoenvironmental Engineering*, *140*(5), 4014002.

Suleiman, M. T., Ni, L., Raich, A., Helm, J., & Ghazanfari, E. (2015). Measured soil–structure interaction for concrete piles subjected to lateral loading. *Canadian Geotechnical Journal*, *52*(8), 1168–1179. https://doi.org/10.1139/cgj-2014-0197

Tamura, S., Adachi, K., Sakamoto, T., Hida, T., & Hayashi, Y. (2012). Effects of existing piles on lateral resistance of new piles. *Soils and Foundations*, *52*(3), 381–392.

Toufigh, V., Abyaneh, M. J., & Jafari, K. (2017). Study of Behavior of Concrete under Axial and Triaxial Compression. *ACI Materials Journal*, *114*(4).

Toufigh, V., Hosseinali, M., & Shirkhorshidi, S. M. (2016). Experimental study and constitutive modeling of polymer concrete's behavior in compression. *Construction and Building Materials*, *112*, 183–190. https://doi.org/10.1016/j.conbuildmat.2016.02.100

Trochanis, A. M., Bielak, J., & Christiano, P. (1991). Three-dimensional nonlinear study of piles. *Journal of Geotechnical Engineering*, *117*(3), 429–447.

Van den Berg, Peter, de Borst, R., & Huétink, H. (1996). An Eulerean finite element model for penetration in layered soil. *International Journal for Numerical and Analytical Methods in Geomechanics*, *20*(12), 865–886.

Van den Berg, Pieter. (1994). *Analysis of soil penetration*. TU Delft, Delft University of Technology.

Wallace, J. W., Fox, P. J., Stewart, J. P., Janoyan, K., Tong, Q., & Lermitte, S. P. (2002). Cyclic large deflection testing of shaft bridges part II: analytical studies. *Report from California Dept. of Transportation*.

Yang, Z., & Jeremić, B. (2002). Numerical analysis of pile behaviour under lateral loads in layered elastic–plastic soils. *International Journal for Numerical and Analytical Methods in Geomechanics*, *26*(14), 1385–1406.

Zarrabi, M., & Eslami, A. (2016). Behavior of piles under different installation effects by physical modeling. *International Journal of Geomechanics*, *16*(5), 4016014.

Zhang, L. M., & Chu, K. H. (2012). Lateral Movements of Long-Driven Piles during Pile Driving. *Journal of Geotechnical and Geoenvironmental Engineering*, *138*(10), 1222–1236. https://doi.org/10.1061/(ASCE)GT.1943-5606.0000707

Zhang, L., Zhao, M., & Zou, X. (2013). Behavior of laterally loaded piles in multilayered soils. *International Journal of Geomechanics*, *15*(2), 6014017.

Zhao, J. (2000). Applicability of Mohr–Coulomb and Hoek–Brown strength criteria to the dynamic strength of brittle rock. *International Journal of Rock Mechanics and Mining Sciences*, *37*(7), 1115–1121.

Zhu, Z., Ahmad, I., & Mirmiran, A. (2006). Seismic performance of concrete-filled FRP tube columns for bridge substructure. *Journal of Bridge Engineering*, *11*(3), 359–370.

Zienkiewicz, O. C., & Taylor, R. L. (2005). *The finite element method for solid and structural mechanics*. Butterworth-heinemann.

APPENDIX A MATLAB Code

main.m

```
close all; clear all; clc; tic

global nnd nel nne nodof eldof ngp gauss_points
global geom connec RE E nu nf dF u du ddu t C_e_concrete C_e_soil D_con
global K_T F_I Eps S dS S_eq S_yield H c phi alpha k
global NRE NZE dhr dhz stp nstp tol R Eps_av C_con g_tol
global dEps R_av S_c A Z b h zero g_0 alpha_penalty g

format long g

nne = 8;
nodof = 3;
eldof = nne*nodof;

mesh;

E_concrete = 3000; % (ksi) , For D-P(I): E =
nu_concrete = 0.25;
E_soil = 200; % (ksi) , For D-P(I): E =
nu_soil = 0.25;
g_0 = zero; % intial gap (in)
t = 2*pi*RE; % (in)
H = 0; % hardening parameter
c = 10; % Cohesion , For D-P(I): c =
phi = 40; % Angle of friction (degree)

alpha_penalty = 1e10; % (ksi)
g_tol = 0.1*zero;
C_con = zeros(1,nodof*nnd);
C_con(1,nodof*(6:46:466)) = -1; % Horizontal part of concrete = -1
C_con(1,nodof*(466:1:506) - 1) = -1; % Vertical part of concrete = -1
C_con(1,nodof*(5:46:465)) = 1; % Horizontal part of soil = 1
C_con(1,nodof*(512:1:552) - 1) = 1; % Vertical part of soil = 1

prompt_user;

%% Forming C_e and D_con matrices

C_e_concrete = form_C_e(E_concrete,nu_concrete);
C_e_soil = form_C_e(E_soil,nu_soil);

%% Defining number of steps

nstp = 20;

%% Defining nodal freedom

nf = ones(nnd,nodof);
for i = 1:NRE+1
    nf(1+(i-1)*(NZE+1),2) = 0; % Bottom Nodes (y)
    %nf(i*(NZE+1),2) = 0; % Top Nodes (y)
```

```
end
nf(1:NZE+1,1) = 0; % Left-hand side Nodes
nf(11*46,1) = 0; % Applied Load Node
nf([543:1:552, 589:1:598, 635:1:644, 681:1:690, 691:1:736],:) = 0; % Removed
Nodes at the top right-hand side of mesh and right side of soil

I = 0;
I_r = 0;
for i = 1:nnd
    for j = 1:nodof
        I = I + 1;
        if nf(i,j) == 0
            I_r = I_r + 1;
            dof_r(I_r) = I;
        end
    end
end

dof_total = 1:nnd*nodof;
dof_ur = setdiff(dof_total,dof_r);

%% Defining nodal loads

F_E = zeros(nnd*nodof,1);

p_z = 0; % Uniformly distributed pressure (ksi)

f_z = p_z * t * b;

for i = 1:NRE
    F_E(nodof*(NZE + (i-1)*(NZE+1) + 1)) = -f_z;
    F_E(nodof*(NZE + i*(NZE+1) + 1)) = -f_z;
end
F_E(nodof*(NZE + 1)) = -f_z/2;
F_E(nodof*(NZE + NRE*(NZE+1) + 1)) = -f_z/2;

% Horizontal_Load = 20; % (kip)

% F_E(nodof*11*46 - 1) = -Horizontal_Load;

dF_E = F_E/nstp;
F_E = cell(1,nstp);
F_E{1,1} = zeros(nnd*nodof,1);

p_r = 0;  % Uniformly distributed pressure (ksi)
f_r = p_r * t * h;

for j = 1:NZE
    F_E{1,1}(nodof*(j + NRE*(NZE+1)) - 1) = -f_r;
    F_E{1,1}(nodof*(j + NRE*(NZE+1) + 1) - 1) = -f_r;
end
F_E{1,1}(nodof*(1 + NRE*(NZE+1)) - 1) = -f_r/2;
F_E{1,1}(nodof*(NZE + NRE*(NZE+1) + 1) - 1) = -f_r/2;

%% Gaussian points
```

```
GP = 1/sqrt(3);

gauss_points = [-GP  -GP  1
                GP   -GP  1
                GP   GP   1
                -GP  GP   1];

ngp = size(gauss_points,1);

%% Initializing

dEps = cell(1,nstp+1);
dEps{1,1} = cell(1,nel);
for el = 1:nel
    for gp = 1:ngp
        dEps{1,1}{1,el}{1,gp} = zeros(4,1);
    end
end

Eps = cell(1,nstp+1);
Eps{1,1} = cell(1,nel);
for el = 1:nel
    for gp = 1:ngp
        Eps{1,1}{1,el}{1,gp} = zeros(4,1);
    end
end

S = cell(1,nstp+1);
S{1,1} = cell(1,nel);
for el = 1:nel
    for gp = 1:ngp
        S{1,1}{1,el}{1,gp} = zeros(4,1);
    end
end

R = cell(1,nstp+1);
for stp = 1:nstp+1
    R{1,stp} = cell(1,nel);
    for el = 1:nel
        R{1,stp}{1,el} = cell(1,ngp);
        for gp = 1:ngp
            R{1,stp}{1,el}{1,gp} = 0;
        end
    end
end

u = cell(1,nstp+1);
u{1,1} = zeros(nnd*nodof,1);
du = zeros(nnd*nodof,1);
ddu = zeros(nnd*nodof,1);

stp = 0;

[Eps{1,1},S{1,1}] = K_T_F_I(Eps{1,1},S{1,1});

%% Starting steps
```

```
for stp = 1:nstp

    stp

    du = zeros(nnd*nodof,1);

    du(nodof*11*46 - 1) = -25/nstp; % (in)

    u_norm(1) = norm(u{1,stp}); % u_norm of first iteration

    F_E{1,stp+1} = F_E{1,stp} + dF_E;

    dF = dF_E(dof_ur,1) - K_T(dof_ur,dof_r)*du(dof_r,1);  % size(dF) =
(dof_ur,1)

    Res{1,1} = dF;

    %% Starting iterations

    iter = 0;
    error = 1;
    tol = 1e-3;
    max_iter = 5;

    while error > tol && iter < max_iter

        iter = iter + 1

        %inv_K_T_ur = inv(K_T(dof_ur,dof_ur));
        %det(K_T(dof_ur,dof_ur))
        %stiffness = K_T(dof_ur,dof_ur);
        ddu(dof_ur,1) = K_T(dof_ur,dof_ur) \ Res{1,iter};
        du(dof_ur,1) = du(dof_ur,1) + ddu(dof_ur,1);
        u{1,stp+1} = u{1,stp} + du;

        u_norm(iter+1) = norm(u{1,stp+1});

        [Eps{1,stp+1},S{1,stp+1}] = K_T_F_I(Eps{1,stp},S{1,stp});

        Res{1,iter+1} = F_E{1,stp+1}(dof_ur,1) - F_I{1,stp+1}(dof_ur,1);

        error = abs( (u_norm(iter+1) - u_norm(iter)) / u_norm(iter) )
        %break
    end
    if stp == 1
    %break
    end
end

%% Organizing results

origanize_results;

time = toc
```

K T F I.m

```
function [Eps,S] = K_T_F_I(Eps,S)

global nnd nel nodof eldof gp gp_con ngp ngp_con stp nstp h
global geom connec C_e_concrete C_e_soil C_ep u du t el D_con
global K_T F_I S_yield dS dEps gauss_points alpha_penalty C_con g_tol
global J1 J2D J3D J1_old J2D_old J3D_old R S_eq_old S_eq tol g g_0

%br = 0;

F_I{1,stp+1} = zeros(nnd*nodof,1);
K_T = zeros(nnd*nodof);

for el = 1:nel

    el;

    [coord,DOF] = total_to_element(el);

    if any(el == [481:1:489, 526:1:534, 571:1:579, 616:1:624])
        continue

    else
        f_I = zeros(eldof,1);
        k_T = zeros(eldof);

        for gp = 1:ngp
            gp;

            [der,fun] = der_fun(gauss_points,gp);
            W = gauss_points(gp,3);
            J = der*coord;
            deriv = J\der;
            %jabejayi_stp_1 = u{1,stp+1}(DOF)
            [B_bar, G] = form_B_bar(deriv,u{1,stp+1}(DOF),fun,coord);
            dEps{1,stp+1}{1,el}{1,gp} = B_bar*du(DOF);
            %dEpsilon = dEps{1,stp+1}{1,el}{1,gp};

            %B = form_B(deriv,fun,coord);
            %dEps{1,stp+1}{1,el}{1,gp} = B*du(DOF);

            if any(el == [5:44, 49:88, 93:132, 137:176, 181:220, 225:264,
269:308, 313:352, 357:396, 401:440]) % Concrete elements
                %disp('2');
                dS = C_e_concrete*dEps{1,stp+1}{1,el}{1,gp};
                D = C_e_concrete;

            elseif any(el == [1:4, 45:48, 89:92, 133:136, 177:180, 221:224,
265:268, 309:312, 353:356, 397:400, 441:444, 445:480, 490:525, 535:570,
580:615]) % Soil elements
                %disp('3');
                dS = C_e_soil*dEps{1,stp+1}{1,el}{1,gp};
                D = C_e_soil;
```

```
            end

            Eps_old{1,el}{1,gp} = Eps{1,el}{1,gp};
            S_old{1,el}{1,gp} = S{1,el}{1,gp};

            [J1_old,J2D_old,J3D_old] = form_invariants(S_old{1,el}{1,gp});
            S_eq_old =
equivalent_stress(J1_old,J2D_old,J3D_old,Eps_old{1,el}{1,gp});

            Eps{1,el}{1,gp} = Eps_old{1,el}{1,gp} +
dEps{1,stp+1}{1,el}{1,gp};
            S{1,el}{1,gp} = S_old{1,el}{1,gp} + dS;

            [J1,J2D,J3D] = form_invariants(S{1,el}{1,gp});
            S_eq{1,stp+1}{1,el}{1,gp} =
equivalent_stress(J1,J2D,J3D,Eps{1,el}{1,gp});

            if stp == 0
                S_eq_old = 0;
                S_eq{1,stp+1}{1,el}{1,gp} = 0;

            else

                if stp == 1
                    S_eq_old = 0;
                end

                if S_eq_old < S_yield && abs( (S_eq_old - S_yield) / S_yield
) > tol
                    %fprintf('gp: %d => S_eq_old < S_yield\n',gp)
                    if S_eq{1,stp+1}{1,el}{1,gp} > S_yield || abs(
(S_eq{1,stp+1}{1,el}{1,gp} - S_yield) / S_yield ) < tol
                        %fprintf('gp: %d => S_eq > S_yield\n',gp)
                        R{1,stp+1}{1,el}{1,gp} = (S_eq{1,stp+1}{1,el}{1,gp} -
S_yield) / (S_eq{1,stp+1}{1,el}{1,gp} - S_eq_old);
                        S{1,el}{1,gp} =
plastic_corrector(Eps{1,el}{1,gp},S_old{1,el}{1,gp},S{1,el}{1,gp});
                        D = C_ep;
                    else
                        %fprintf('gp: %d => S_eq < S_yield\n',gp)
                    end

                else
                    %fprintf('gp: %d => S_eq_old > S_yield\n',gp)
                    if S_eq{1,stp+1}{1,el}{1,gp} > S_yield  || abs(
(S_eq{1,stp+1}{1,el}{1,gp} - S_yield) / S_yield ) < tol
                        %fprintf('gp: %d => S_eq > S_yield\n',gp)
                        R{1,stp+1}{1,el}{1,gp} = 1;
                        S{1,el}{1,gp} =
plastic_corrector(Eps{1,el}{1,gp},S_old{1,el}{1,gp},S{1,el}{1,gp});
                        D = C_ep;
                    else
                        %fprintf('gp: %d => S_eq < S_yield\n',gp)
                    end
                end
            end
```

```
            M_s = form_M_s(S{1,el}{1,gp});

            f_I = f_I + det(J)*W*t*B_bar'*S{1,el}{1,gp};
            k_T = k_T + det(J)*W*t*B_bar'*D*B_bar + det(J)*W*t*G'*M_s*G;

            %f_I = f_I + det(J)*W*t*B'*S{1,el}{1,gp};
            %k_T = k_T + det(J)*W*t*B'*D*B;

        end

        F_I{1,stp+1}(DOF) = F_I{1,stp+1}(DOF) + f_I;
        K_T(DOF,DOF) = K_T(DOF,DOF) + k_T;

    end
end

for i = 1:11 % Horizontal contact nodes
    I_con = [nodof*(5 + (i-1)*46), nodof*(6 + (i-1)*46)];
    g{1,stp+1}(i) = C_con(I_con) * u{1,stp+1}(I_con) - g_0;

    if abs(g{1,stp+1}(i)/geom(5 + (i-1)*46,2)) < g_tol
        K_T(I_con,I_con) = K_T(I_con,I_con) +
C_con(I_con)'*alpha_penalty*C_con(I_con);
    end
end

for i = 1:32 % Vertical contact nodes
    I_con = [nodof*(466 + i - 1) - 1, nodof*(512 + i - 1) - 1];
    g{2,stp+1}(i) = C_con(I_con) * u{1,stp+1}(I_con) - g_0;

    if abs(g{2,stp+1}(i)/geom(466 + i - 1,1)) < g_tol
        K_T(I_con,I_con) = K_T(I_con,I_con) +
C_con(I_con)'*alpha_penalty*C_con(I_con);
    end
end
```

DSC.m

```
global nstp dEps_av Eps_av S_eq_av R_av Eps_c S_c A Z Eps_prediction
S_prediction

D_u = 1;
Z = 1.4;
A = 350;

eksi_D{1,1} = 0;
D{1,1} = 0;
Eps_prediction(1,1:4) = 0;
S_prediction(1,1) = 0;
for stp = 2:nstp+1
    dEps_m = [dEps_av(stp,1)       dEps_av(stp,3)      0
              dEps_av(stp,3)       dEps_av(stp,2)      0
              0                    0                   dEps_av(stp,4)];

    dEps_m_P = R_av(stp,1)*dEps_m;  % Plastic strain matrix
```

```
    dEps_m_P_D = dEps_m_P - (1/3)*trace(dEps_m_P)*eye(3);  % Deviatoric
plastic strain matrix

    eksi_D{1,stp} = eksi_D{1,stp-1} + norm(dEps_m_P_D);

    D{1,stp} = D_u*(1 - exp(-A*(eksi_D{1,stp}^Z)));

    dEps_prediction = (1 - D{1,stp})*(Eps_av(stp,:) - Eps_av(stp-1,:)) +
(D{1,stp} - D{1,stp-1})*(Eps_c - Eps_av(stp-1,:));
    dS_prediction = (1 - D{1,stp})*(S_eq_av(stp,1) - S_eq_av(stp-1,1)) +
(D{1,stp} - D{1,stp-1})*(S_c - S_eq_av(stp-1,1));

    Eps_prediction(stp,:) = Eps_prediction(stp-1,:) + dEps_prediction;
    S_prediction(stp,1) = S_prediction(stp-1,1) + dS_prediction;
end
```

organize_results.m

```
global nstp nnd nel nne nodof ngp ngp_con dEps_av dEps Eps S S_eq R Eps_node
S_node S_eq_node R_node Eps_av S_av S_eq_av R_av u

dEps_av = zeros(nstp+1,4);
Eps_av = zeros(nstp+1,4);
S_av = zeros(nstp+1,4);
S_eq_av = zeros(nstp+1,1);
R_av = zeros(nstp+1,1);
%F_I_z_av = zeros(nstp+1,1);

for stp = 1:nstp+1
    stp;

    for el = 1:nel
        el;

        if any(el == [5:45:455, 456:1:486]) % Contact elements
            dEps_el{1,stp}{1,el} = zeros(2,1);
            Eps_el{1,stp}{1,el} = zeros(2,1);
            S_el{1,stp}{1,el} = zeros(2,1);
            S_eq_el{1,stp}{1,el} = 0;
            R_el{1,stp}{1,el} = 0;

            for gp_con = 1:ngp_con
                dEps_el{1,stp}{1,el} = dEps_el{1,stp}{1,el} +
dEps{1,stp}{1,el}{1,gp_con};
                Eps_el{1,stp}{1,el} = Eps_el{1,stp}{1,el} +
Eps{1,stp}{1,el}{1,gp_con};
                S_el{1,stp}{1,el} = S_el{1,stp}{1,el} +
S{1,stp}{1,el}{1,gp_con};
                %S_eq_el{1,stp}{1,el} = S_eq_el{1,stp}{1,el} +
S_eq{1,stp}{1,el}{1,gp_con}; % S_eq has not been defined for contact elements
                %R_el{1,stp}{1,el} = R_el{1,stp}{1,el} +
R{1,stp}{1,el}{1,gp_con};
            end
```

```
        elseif any(el == [487:1:495, 532:1:540, 577:1:585, 622:1:630,
667:1:675])
            continue

        else
            dEps_el{1,stp}{1,el} = zeros(4,1);
            Eps_el{1,stp}{1,el} = zeros(4,1);
            S_el{1,stp}{1,el} = zeros(4,1);
            S_eq_el{1,stp}{1,el} = 0;
            R_el{1,stp}{1,el} = 0;

            for gp = 1:ngp
                dEps_el{1,stp}{1,el} = dEps_el{1,stp}{1,el} +
dEps{1,stp}{1,el}{1,gp};
                Eps_el{1,stp}{1,el} = Eps_el{1,stp}{1,el} +
Eps{1,stp}{1,el}{1,gp};
                S_el{1,stp}{1,el} = S_el{1,stp}{1,el} + S{1,stp}{1,el}{1,gp};
                S_eq_el{1,stp}{1,el} = S_eq_el{1,stp}{1,el} +
S_eq{1,stp}{1,el}{1,gp};
                R_el{1,stp}{1,el} = R_el{1,stp}{1,el} + R{1,stp}{1,el}{1,gp};
            end
        end

        dEps_el{1,stp}{1,el} = dEps_el{1,stp}{1,el}/ngp;
        Eps_el{1,stp}{1,el} = Eps_el{1,stp}{1,el}/ngp;
        S_el{1,stp}{1,el} = S_el{1,stp}{1,el}/ngp;
        S_eq_el{1,stp}{1,el} = S_eq_el{1,stp}{1,el}/ngp;
        R_el{1,stp}{1,el} = R_el{1,stp}{1,el}/ngp;
    end

    if el == 496
    break
    end

    for nd = 1:nnd
        ne = 0;

        for iel = 1:nel
            for jel = 1:nne
                if connec(iel,jel) == nd
                    iel;
                    jel;

                    if any(iel == [5:45:455, 456:1:486]) % Contact elements
(we don't want to sum these values w/ other values)
                        dEps_node{1,stp}{1,nd} = zeros(2,1);
                        Eps_node{1,stp}{1,nd} = zeros(2,1);
                        S_node{1,stp}{1,nd} = zeros(2,1);
                        S_eq_node{1,stp}{1,nd} = 0;
                        R_node{1,stp}{1,nd} = 0;

                    elseif any(iel == [487:1:495, 532:1:540, 577:1:585,
622:1:630, 667:1:675])
                        continue

                    else
                        ne = ne + 1;
```

```
                        dEps_node{1,stp}{1,nd} = zeros(4,1);
                        Eps_node{1,stp}{1,nd} = zeros(4,1);
                        S_node{1,stp}{1,nd} = zeros(4,1);
                        S_eq_node{1,stp}{1,nd} = 0;
                        R_node{1,stp}{1,nd} = 0;
                    end

                    dEps_node{1,stp}{1,nd} = dEps_node{1,stp}{1,nd} +
dEps_el{1,stp}{1,iel};
                    Eps_node{1,stp}{1,nd} = Eps_node{1,stp}{1,nd} +
Eps_el{1,stp}{1,iel};
                    S_node{1,stp}{1,nd} = S_node{1,stp}{1,nd} +
S_el{1,stp}{1,iel};
                    S_eq_node{1,stp}{1,nd} = S_eq_node{1,stp}{1,nd} +
S_eq_el{1,stp}{1,iel};
                    R_node{1,stp}{1,nd} = R_node{1,stp}{1,nd} +
R_el{1,stp}{1,iel};
                end
            end
        end

            dEps_node{1,stp}{1,nd} = 0;
            Eps_node{1,stp}{1,nd} = 0;
            S_node{1,stp}{1,nd} = [0;0];
            S_eq_node{1,stp}{1,nd} = 0;
            R_node{1,stp}{1,nd} = 0;

            dEps_node{1,stp}{1,nd} = dEps_node{1,stp}{1,nd}/ne;
            Eps_node{1,stp}{1,nd} = Eps_node{1,stp}{1,nd}/ne;
            S_node{1,stp}{1,nd} = S_node{1,stp}{1,nd}/ne;
            S_eq_node{1,stp}{1,nd} = S_eq_node{1,stp}{1,nd}/ne;
            R_node{1,stp}{1,nd} = R_node{1,stp}{1,nd}/ne;
    end

    %u_z41(stp,1) = u{1,stp}(nodof*41,1);
    for nd = 1:nnd
        dEps_av(stp,:) = dEps_av(stp,:) - (dEps_node{1,stp}{1,nd})';
        Eps_av(stp,:) = Eps_av(stp,:) - (Eps_node{1,stp}{1,nd})';
        S_av(stp,:) = S_av(stp,:) - S_node{1,stp}{1,nd}(2);
        S_eq_av(stp,1) = S_eq_av(stp,1) + S_eq_node{1,stp}{1,nd};
        R_av(stp,1) = R_av(stp,1) + R_node{1,stp}{1,nd};
        %F_I_z_av(stp,1) = F_I_z_av(stp,1) + F_I{1,stp}(nodof*i,1);
    end

    dEps_av(stp,:) = dEps_av(stp,:)/nnd;
    Eps_av(stp,:) = Eps_av(stp,:)/nnd;
    S_av(stp,:) = S_av(stp,:)/nnd;
    S_eq_av(stp,1) = S_eq_av(stp,1)/nnd;
    R_av(stp,1) = R_av(stp,1)/nnd;
    %F_I_z_av(stp,1) = F_I_z_av(stp,1)/nnd;
end
```